Applied Geochemistry 132 (2021) 105023

Contents lists available at ScienceDirect

Applied Geochemistry

journal homepage: www.elsevier.com/locate/apgeochem

Effects of mineralogy, chemistry and physical properties of basalts on carbon capture potential and plant-nutrient element release via enhanced weathering

Amy L. Lewis [a,*], Binoy Sarkar [b], Peter Wade [a], Simon J. Kemp [c], Mark E. Hodson [d], Lyla L. Taylor [a], Kok Loong Yeong [a,e], Kalu Davies [g], Paul N. Nelson [g], Michael I. Bird [g], Ilsa B. Kantola [h,i], Michael D. Masters [h,i], Evan DeLucia [h,i], Jonathan R. Leake [a], Steven A. Banwart [j], David J. Beerling [a]

[a] Leverhulme Centre for Climate Change Mitigation, Department of Animal and Plant Sciences, University of Sheffield, Sheffield, S10 2TN, UK
[b] Lancaster Environment Centre, Lancaster University, Lancaster, LA1 4YQ, UK
[c] British Geological Survey, Environmental Science Centre, Keyworth, Nottingham, NG12 5GG, UK
[d] Department of Environment and Geography, University of York, York, YO10 5NG, UK
[e] South East Asia Rainforest Research Partnership, Danum Valley Field Centre, Lahad Datu, Sabah, 91112, Malaysia
[g] College of Science and Engineering and Centre for Tropical Environmental and Sustainability Science, James Cook University, Cairns, Queensland, 4870, Australia
[h] Institute for Sustainability, Energy, and Environment, University of Illinois at Urbana-Champaign, Urbana, IL, 61801, USA
[i] Carl R. Woese Institute for Genomic Biology, University of Illinois at Urbana-Champaign, Urbana, IL, 61801, USA
[j] Global Food and Environment Institute, University of Leeds, Leeds, LS2 9JT, UK

ARTICLE INFO

Editorial handling by Dr. Domenik Wolff-Boenisch

Keywords:
Enhanced rock weathering
Carbon dioxide removal potential
Soil rock amendments
Mineralogy
Surface area analysis
Geochemical modelling

ABSTRACT

Mafic igneous rocks, such as basalt, are composed of abundant calcium- and magnesium-rich silicate minerals widely proposed to be suitable for scalable carbon dioxide removal (CDR) by enhanced rock weathering (ERW). Here, we report a detailed characterization of the mineralogy, chemistry, particle size and surface area of six mined basalts being used in large-scale ERW field trials. We use 1-D reactive transport modelling (RTM) of soil profile processes to simulate inorganic CDR potential via cation flux (Mg^{2+}, Ca^{2+}, K^{+} and Na^{+}) and assess the release of the essential plant nutrients phosphorus (P) and potassium (K) for a typical clay-loam agricultural soil. The basalts are primarily composed of pyroxene and plagioclase feldspar (up to 71 wt%), with accessory olivine, quartz, glass and alkali feldspar. Mean crushed particle size varies by a factor of 10, owing to differences in the mining operations and grinding processes. RTM simulations, based on measured mineral composition and N_2-gas BET specific surface area (SSA), yielded potential CDR values of between *c.* 1.3 and 8.5 t CO_2 ha^{-1} after 15 years following a baseline application of 50 t ha^{-1} basalt. The RTM results are comparative for the range of inputs that are described and should be considered illustrative for an agricultural soil. Nevertheless, they indicate that increasing the surface area for slow-weathering basalts through energy intensive grinding prior to field application in an ERW context may not be warranted in terms of additional CDR gains. We developed a function to convert CDR based on widely available and easily measured rock chemistry measures to more realistic determinations based on mineralogy. When applied to a chemistry dataset for >1300 basalt analyses from 25 large igneous provinces, we simulated cumulative CDR potentials of up to *c.* 8.5 t CO_2 ha^{-1} after 30 years of weathering, assuming a single application of basalt with a SSA of 1 m^2 g^{-1}. Our RTM simulations suggest that ERW with basalt releases sufficient phosphorus (P) to substitute for typical arable crop P-fertiliser usage in Europe and the USA offering potential to reduce demand for expensive rock-derived P.

* Corresponding author.
E-mail address: allewis2@sheffield.ac.uk (A.L. Lewis).

https://doi.org/10.1016/j.apgeochem.2021.105023
Received 1 February 2021; Received in revised form 27 May 2021; Accepted 31 May 2021
Available online 21 June 2021

Table 1
Origin and geological background of the commercially available basalts analysed.

Material	Geological Setting, (age)	Reference	Country of origin	Source and Supplier	Size fraction	Mining technique	Source
Blue Ridge	Metamorphosed basalt. Potentially part of the Catoctin greenstone. Virginia, USA. (Neo-Proterozoic).	USGS (2019)	USA	Purchased from Rock Dust Local LLC, Bridport, Vermont, USA.	<1.34 mm	Collected as fine dust from crushing stages and baghouse dust collection from hard-rock drilling processes.	Mineralogy and particle size distribution, published in Blanc-Betes et al., 2021
Cragmill	Whin Sill (dolerite) emplacement, Pennsylvanian (Carboniferous).	Sabine et al. (1954)	UK	Donated by CEMEX Group, Cragmill, Northumberland.	<4 mm (<15% > 4 mm)	Jaw and cone crushed, then sorted by screening.	This paper
Hillhouse	Intrusive analcime gabbro.	Kirstein et al. (2006)	UK	Donated by Hillhouse Quarry Group, Dundonald, Troon.	<4 mm	Jaw and cone crushed, then sorted by screening.	This paper
Oregon	'Prineville Chemical Type Unit' of the Columbia River Basalt Group. (Middle Miocene).	Smith and Hayman (1987)	USA	Purchased from Central Oregon Basalt Products LLC, Madras, Oregon, USA.	<1.18 mm	Crushed and sorted by screening. Ultrafines removed via dust handling system.	Mineralogy and glass chemistry (SEM-EDS) published in Kelland et al. (2020)
Tawau	Associated with magmatic-arc volcanism (Pleistocene).	Tahir et al. (2010)	Malaysia	Donated by Onika Quarry Co., Tawau, Sabah, Malaysia.	<5 mm (<3% > 5 mm)	Jaw and cone crushed, then sorted by screening.	This paper
Tichum	Associated with continental-mantle plume magmatism (Miocene).	Stephenson et al. (2007)	Australia	Donated by Boral Quarries, Tichum Creek, Queensland, Australia.	<4.75 mm	Jaw and cone crushed, then sorted by screening.	This paper

1. Introduction

The UNFCCC Paris Agreement aims to limit human-caused climate warming to less than 1.5 °C above pre-industrial temperatures. This requires urgent phase-down of CO_2 emissions (IPCC, 2018), and large-scale deployment of safe, effective and environmentally acceptable CO_2 removal (CDR) strategies, on the order of up to 2–10 $GtCO_2$ yr^{-1} by 2050 (Mercure et al., 2018; Rockström et al., 2017). Enhanced rock weathering (ERW) is a proposed CDR strategy that involves accelerating natural carbon sequestration processes driven by chemical weathering of silicate rocks (e.g. Lackner et al., 1995; Seifritz, 1990). During chemical weathering of silicate rocks, dissolved atmospheric CO_2 forms aqueous species that accelerate the dissolution of silicate phases (minerals and glasses) with proton consumption to generate bicarbonate (Eq. (1)). Eventually, this bicarbonate is transported to the oceans via runoff where it is stored in a stable form for approximately ~100,000 years (Renforth and Henderson, 2017):

$$CaMgSi_2O_6 + 4CO_2(g) + 6H_2O \rightarrow Mg^{2+} + Ca^{2+} + 2H_4SiO_4 + 4HCO_3^- \quad (1)$$

Bicarbonate carbon may be precipitated as pedogenic carbonates, depending on soil pH, which leads to a net of 1 mol of CO_2 being captured for every 2 mol of CO_2 consumed in the silicate weathering reaction (Eq. (2)):

$$Ca^{2+} + 2HCO_3^- \rightarrow CaCO_3 + H_2O + CO_2(g) \quad (2)$$

Land-based ERW can involve amending forest (Köhler et al., 2010; Strefler et al., 2018; Taylor et al., 2015) and cropland (Beerling et al, 2018, 2020; Kantola et al., 2017) soils with finely-crushed silicate rocks. Basalt, an abundant, fast-weathering, Ca- and Mg-rich, silicate rock, is considered a prime candidate for ERW (Beerling et al, 2018, 2020). The major constituent minerals of basalt (pyroxenes, olivine and plagioclase feldspar) typically weather faster, and can therefore potentially capture CO_2 faster, than minerals commonly found in granitic or sedimentary rocks (e.g. quartz, K-feldspar, muscovite) (Palandri and Kharaka, 2004). Finely crushed basalt is an abundant by-product of the aggregate and mining industry and there is growing recognition of its potential to improve soil health and support crop production (D'Hotman and De Villers, 1961; Gillman et al., 2002; Kelland et al., 2020; Ramos et al., 2019). The increased reactive surface area per unit volume of crushed basalt accelerates dissolution compared to natural *in situ* outcrops. Basalt weathering also liberates inorganic plant nutrients, including Ca, Mg, Fe, K, P and micronutrients (e.g., Mo), that could support crop production and generate alkalinity to reverse soil acidification caused by agricultural production (Beerling et al., 2018; Hartmann et al., 2013; Kantola et al., 2017). If crop biomass is not returned to fields following harvest, major cations taken up from the soil (Ca^{2+}, Mg^{2+}, K^+) during growth will be unavailable to contribute to CDR via alkalinity production in soil pore waters (Banwart et al., 2009).

Basalts are formed following eruption in a variety of tectonic environments, and differences in petrogenesis result in a range of mineralogical compositions. Basalt diagnostically contains pyroxene- (e.g. diopside and augite) and plagioclase feldspar-group minerals (e.g. andesine, labradorite, bytownite and anorthite) (Wilson, 1989). The identity and proportion of accessory minerals may also vary, depending on the melt chemistry (e.g. olivine from Fe- and Mg-rich magmas, amphibole from hydrated magma). Rapid quenching of the melt can lead to basaltic glass formation (Allen et al., 1981). Secondary minerals (e.g. saponite, various zeolites) may form during hydrothermal alteration and weathering of basalts (Kristmannsdottir, 1979).

The dissolution rate of minerals is a function of their surface area and dissolution rate constants as well as temperature and solution composition, including pH. Mineral dissolution rate is described in Eq. (3) (Declercq and Oelkers, 2014; Palandri and Kharaka, 2004):

$$\frac{dm}{dt} = -SA \cdot \begin{bmatrix} A_{acid} e^{\frac{-E_{acid}}{RT}} \cdot a_{H+}^{n_{acid}} \cdot (1 - SR) \\ + A_{neutral} e^{\frac{-E_{neutral}}{RT}} \cdot (1 - SR) \\ + A_{base} A e^{\frac{-E_{base}}{RT}} \cdot a_{H+}^{n_{base}} \cdot (1 - SR) \end{bmatrix} \quad (3)$$

Where m is the number of moles of the mineral, t is time (in seconds, s), SA is the surface area, A is the pre-exponential factor (the rate constant) of the acid, neutral and base dissolution mechanism, E is the activation energy of the acid, neutral and base dissolution mechanism, R is the gas constant for water (8.31, J mol^{-1} K^{-1}), T is the temperature in Kelvin, K, a is the ion activity of hydrogen (H^+), n is the reaction order for the acid, neutral and base dissolution mechanism, and SR is the saturation ratio. In addition to mineralogy, surface area (SA, Eq. (3)) is a crucial variable in the dissolution rate equation and is controlled by particle size, particle roughness, and mineralogy (Brantley et al., 1999; Parry et al., 2015). The particle size of crushed rocks varies depending on the rock composition and processing procedures used by mining companies and is the most energy intensive step in the ERW supply chain (Beerling

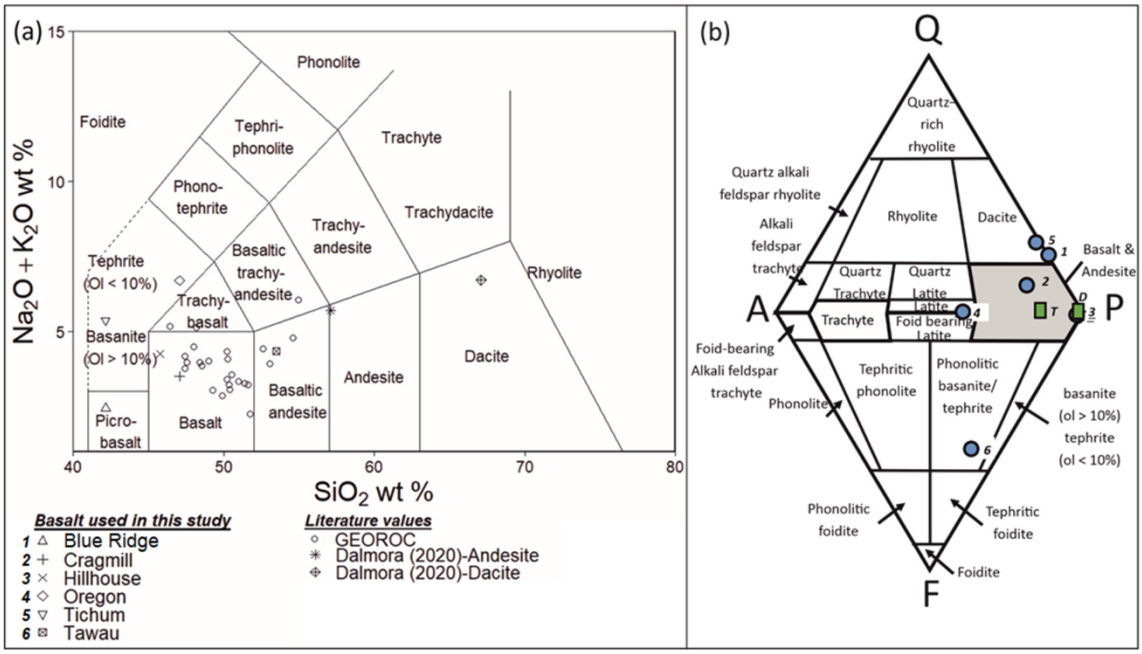

Fig. 1. Total Alkaline Silica (TAS) (a) and Quartz Alkali Plagioclase Feldspathoid (QAPF) (b) classifications of the six materials studied. Circles in Fig. 1a denote average alkaline ($Na_2O + K_2O$ wt%) and SiO_2 wt% data collated from continental flood basalts and large igneous provinces (n = 25) from the GEOROC database (Sarbas, 2008). In Fig. 1b, numbers for each basalt are shown in the legend of Fig. 1a, with the exception of T and D (position marked with green squares) which correspond to basalt used in model simulations in Taylor et al. (2015) and dissolution experiments in Dontsova et al. (2014) respectively. (For interpretation of the references to colour in this figure legend, the reader is referred to the Web version of this article.)

et al., 2020; Moosdorf et al., 2014; Renforth, 2012). However, utilizing mineralogically suitable silicate quarry fines from mining companies will reduce the dependency on energy intensive crushing. These fines are also recognized as valuable feed-stocks for sequestering CO_2 to assist in developing strategies for carbon neutral mining (Power et al., 2014).

Here, we report detailed mineralogical (X-ray diffraction; XRD), chemical (Scanning Electron Microscopy - Energy Dispersive Spectroscopy; SEM-EDS and Inductive Coupled Plasma - Optical Emission Spectroscopy; ICP-OES), particle size (laser particle size analysis and mass fraction sieving) and surface area (Brunauer, Emmet, Teller (BET)-N_2 adsorption) characterisation of six basalts, as quarry fines from mining companies, being trialled across a worldwide network of large-scale ERW-CDR field-trial sites. We then use this mineralogical and surface area data in reactive transport modelling (RTM) to (1) evaluate the relative importance of mineralogy and particle surface area for CDR, (2) derive a function to predict the CDR potential of a basalt based on its chemical composition and surface area, and (3) track the release of essential plant nutrients P and K during dissolution to determine the potential of ERW with basalt to substitute for P and K fertilizers derived from finite high-grade mineral reserves (Amann and Hartmann, 2019; Amundson et al., 2015; Beerling et al., 2020; Ciceri et al., 2015; Elser and Bennett, 2011).

2. Methods

We analysed basalts sourced from six commercial quarries extracting basalt that formed during hotspot and crustal extension-related episodes (Oregon, Tichum, Cragmill and Hillhouse), island arc magmatism (Tawau) and medium temperature and pressure regional metamorphism (Blue Ridge) (Table 1). Several of the materials we investigated were not formally classified as basalts, but they are mostly mafic in origin. Therefore, for simplicity, we collectively refer to all materials here as basalts with the exception of the Blue Ridge which we refer to as a metabasalt. All basalts, except the Blue Ridge metabasalt, were processed following conventional crushing and screening techniques at the quarry sites (Table 1). The Oregon basalt underwent additional on-site processing through air-extraction systems, limiting the abundance of finer particles (<75 μm). The Blue Ridge metabasalt comprised fine dust collected from the air during the commercial crushing process.

2.1. Basalt chemistry and mineralogy

For chemical and mineralogical analyses, basalt samples were pulverized in a Fritsch Pulverisette agate ball mill (Fritsch International, Oberstein, Germany), then ground further using a pestle and mortar to homogenise the sample to <125 μm. Elemental chemistry was determined using Inductively Coupled Plasma - Optical Emission Spectroscopy (ICP-OES) (Faculty of Science, University of Sheffield) on HF-digested powdered samples of 0.25 g. The spectrometer was calibrated with elemental standards between 1 and 25 mg L^{-1} (Spex Certiprep, Rickmansworth - UK), with typical accuracy within ±2% error of the measured value.

The mineralogy of the basalts was determined using X-ray diffraction (XRD) analysis at the British Geological Survey (BGS) Keyworth laboratories. Samples were spiked with 10 wt% corundum (Al_2O_3), micronised to aid quantitative analysis and spray-dried from an ethanol suspension at 80 °C to ensure random orientation of mineral phases (Hillier, 1999). Measurements were conducted using a PANalytical X'Pert Pro diffractometer (Malvern Panalytical Ltd., Malvern, UK) equipped with Co-Kα radiation (λ = 1.78896 Å) and operated at 45 kV and 40 mA. Front-loaded powder mounts were scanned from 4.5 to 85°2θ at 2.06°2θ/minute. Crystalline mineral phases were identified using PANalytical HighScore Plus software (v. 4.8) coupled to the International Centre for Diffraction Data PDF-4+ database (International Centre for Diffraction Data (ICDD), 2019). Crystalline mineral and amorphous material quantification was completed using the Rietveld refinement technique within the same HighScore Plus software package using crystallographic information from the Inorganic Crystal Structure Database (Hellenbrandt, 2004; Inorganic Crystal Structure Database (ICSD), 2019) following the methodology in Kemp et al. (2016a).

2.1.1. Clay mineralogy

Fine fraction separations and further XRD analyses were conducted to definitively identify any clay minerals present and therefore aid the powder mount interpretations. The clay-sized (<2 μm) fractions were isolated by settling and dried following the protocol of Kemp et al. (2016b). The dried clay separates (*c.* 20 mg) were weighed into test tubes with *c.* 0.5 mL of deionised water and 2 drops of 0.1 M calcium chloride hexahydrate ($CaCl_2.6H_2O$) and ultrasonicated for 1 h to fully disperse the particles. The resulting suspensions were pipetted onto zero-background silicon crystal substrates to produce oriented mounts. The mounts were then slowly dried at room temperature to prevent cracking.

The clay separates were characterised by subjecting the oriented mounts to standard diagnostic tests and repeated XRD scans from 2° to 40°2θ at 1.02°2θ/minute: (1) after air-drying, (2) after overnight ethylene glycol (EG) solvation at 55 °C (smectite identification), and (3) after heating to 550 °C for 2 h (kaolinite identification; Moore and Reynolds, 1997). XRD traces were interpreted by comparison of sample peak *d*-spacings and relative intensities with standard values (Moore and Reynolds, 1997).

2.2. Scanning electron microscopy

Scanning electron microscopy (SEM) was used to assess the textural characteristics of the samples including morphology, sizes and the relative relationships between the different grains; chemical compositions were also determined. For this, the basalt particles were mounted in epoxy resin blocks and polished prior to analysis. Detailed mineralogical observations were made on both the polished blocks and on stub-mounted samples. Both blocks and stubs were carbon coated to approximately 25 nm thickness in an Agar AGB7367A automatic SEM carbon evaporation coater, prior to analysis.

Image acquisition for both polished block and stub-mounted sample analysis was performed using a FEI QUANTA 600 SEM at the BGS laboratories, operating at an accelerating voltage of 20 kV. For polished block analysis, a beam current of 2.3 nA and under high vacuum conditions (<1x10 $^{-4}$ Torr). Reduced beam currents of 0.081 and 0.31 nA were used for imaging the stub-mounted samples under high vacuum conditions with the exception of the Tichum basalt which frequently developed charge when imaged under high vacuum and was subsequently imaged in low vacuum mode. Energy Dispersive X-ray Spectroscopy (EDS) analysis was conducted using an Oxford Instruments X-MAX large area (50 mm^2) silicon drift detector (SDD), running with Oxford Instruments INCA (v4) software. The EDS system was used to

Table 2
Rate constants of the minerals identified in the basalts, and the relative proportions of fast, medium and slow weathering silicate minerals. Rate constants are taken from Palandri and Kharaka (2004).

Reactivity grouping (from rate constants)	Mineral	Rate constant, A, H^+	Rate constant, A, H_2O	Relative proportion of 'mineral reactivity' groupings (based on rate constants)					
Silicate minerals				**Blue Ridge**	**Cragmill**	**Hillhouse**	**Oregon**	**Tichum**	**Tawau**
Fast				11.6%	66.6%	82.0%	70.6%	86.1%	57.0%
	Plagioclase (Ca/Na rich) - Labradorite[a] - Andesine[a]	−8.88 to −7.87	−11.47 to −10.91						
	Ferroactinolite	−8.40	−10.6						
	Leucite	−6.00	−9.20						
	Diopside	−6.36	−11.11						
	Augite	−6.82	−11.97						
	Olivine	−6.85	−10.64						
	Basaltic glass	−3.30	−11.85						
	Cordierite	−3.80	−11.20						
Medium				81.5%	11.4%	–	23.0%	2.4%	13.3%
	Plagioclase (Na-rich) - Albite[a]	−10.16	−12.56						
	Epidote	−10.60	−11.99						
	Clinochlore	−11.11	−12.52						
	Sanidine	−10.06	−12.41						
	Orthoclase	−10.06	−12.41						
Slow				5.2%	17.3%	5.2%	1.6%	–	24.9%
	Quartz	−13.99	−16.29						
	Chlorite-Smectite	−12.71[b]	−14.41[b]						
	Smectite	−12.71	−14.41						
	Kaolinite	−11.31	−13.18						
Unknown				–	–	11.5%	–	5.8%	1.0%
	Analcime	NA[c]	NA[c]						
	Epistibite	NA[c]	NA[c]						
	Spinel	NA[c]	NA[c]						
Other minerals/trace silicates									
Fast	Calcite	−0.30	−5.81						
	Apatite	−3.73	−8.00						
	Ilmenite	−8.35	−11.16						
	Hematite	−9.39	−14.60						
	Magnetite	−8.59	−10.78						
Medium	Biotite	−9.84	−12.55						
Unknown	Titanite	NA[c]	NA[c]						
	Phlogopite	NA[c]	−12.40						

[a] Mineralogical analyses identify the plagioclase feldspars as: albite in the Blue Ridge; labradorite in the Cragmill, Hillhouse and Tawau; andesine in the Oregon and Tichum.
[b] Assuming dissolution rate constant of montmorillonite.
[c] We are not aware of dissolution rate data for these minerals.

Table 3
Calcite concentrations derived from thermogravimetric analysis (TGA).

Basalt	Calcite (wt%)
Blue Ridge	0.540
Cragmill	1.249
Hillhouse	0.195
Oregon	0.173
Tawau	0.642
Tichum	0.223

Table 4
Whole rock specific surface areas (SSA) as determined by N_2-adsorption and the BET isotherm (BET SSA) (±standard error), mean particle sizes (Geometric SSA) and surface roughness.

Sample	BET SSA, m^2g^{-1}	Geometric SSA, m^2g^{-1}	Surface Roughness, λ
Blue Ridge	1.02 ± 0.014	0.077	13.21
Cragmill	1.01 ± 0.052	0.018	55.84
Hillhouse	1.39 ± 0.072	0.015	92.85
Oregon	14.54 ± 0.29	0.006	2423.23
Tawau	2.73 ± 0.057	0.011	248.76
Tichum	10.30 ± 0.396	0.01	1029.83

identify and semi-quantitatively measure the elements (from atomic number 5 (B) to 92 (U)) at the selected point of interest with a detection limit of 0.2–0.5 wt % for most elements. Images were obtained with secondary electron (SE) and backscatter electron (BSE) imaging techniques.

Minerals were identified from mineral form observations and EDS spectra. Minerals with solid solution chemistries (e.g. feldspar), containing appreciable trace elements (e.g. pyroxenes), or that were rare (e.g. titanite), were identified through comparison of measured elemental weight percentages to those of known minerals using Webmineral Element Composition Search (Webmineral, 2019).

Chemical data from point analyses were compiled into R (R Development Core Team, 2018) to compute the average composition of the different mineral types identified using SEM-EDS. The EDS analyses are considered semi-quantitative and as a result were normalised to ideal mineral formulae reported in the Handbook of Mineralogy (Anthony et al., 1995). Elements with concentrations below 1% were discounted from the mineral formula calculation. Amorphous phases, interpreted as basaltic glass, were normalised to Si concentrations. The average measured mineral compositions obtained from SEM-EDS were used to select appropriate crystallographic information files for XRD quantification from the Inorganic Crystal Structure Database (Hellenbrandt, 2004; Inorganic Crystal Structure Database (ICSD), 2019).

2.3. Particle size analysis

Particle size analysis was conducted so that geometric surface area could be calculated. Two methods were used: (1) mass fraction sieving on entire basalt samples, and (2) laser particle size analysis of a sieved <75 μm fraction. Mass fraction sieving was carried out to determine the distributions of larger particles (>75 μm) likely to be missed by laser particle size analysis due to rapid particle settling. Data from both methods were combined, with particles identified to be larger than 75 μm from laser particle size analysis discounted from the overall particle size distribution. Geometric specific surface area (SSA) was calculated as described in Kelland et al. (2020) (see Supplementary Information, Table S3 in Kelland et al. (2020)).

2.3.1. Mass fraction sieving

Representative sub-samples, between 30 and 40 g (18–20 g Blue Ridge), were produced by coning, quartering, and riffle-splitting. A smaller mass of the Blue Ridge metabasalt was used as its comparatively fine-grain size clogged the sieves. Samples were sieved through 4000, 2000, 1000, 500, 250, 180, 125 and 75 μm sieves using a Retsch AS200 sieve shaker for 5 min (2 × 5 min for the Blue Ridge to prevent clogging) and the mass of each size fraction recorded.

2.3.2. Laser particle size analysis

The <75 μm mass fraction was riffle split to produce a representative sample and particle size was determined using a Horiba LA950 Partica Laser Scattering Particle Size Analyser (Horiba UK Ltd, Northampton, UK). The samples were fully dispersed into suspension using 0.1 M sodium hexametaphosphate solution and ultra-sonication for 1 min before measurement.

2.4. Basalt BET surface area analysis

The specific surface area of the samples was determined using N_2 adsorption and application of the BET isotherm (Brunauer et al., 1938). For this, the samples were sieved to <4 mm prior to analysis to fit into the measurement tubes. The <4 mm fraction was split into *c.* 2.5 g subsamples using a riffle splitter. Subsamples were degassed overnight in a Micrometrics VacPrep 061 Sample Degas System at 60 °C and *c.* 200 mTorr to remove residual water and gas. The sample weight after degassing was recorded and incorporated into surface area calculations. Surface area analyses were conducted using a Micromeritics Gemini VI 2385C system at the BGS laboratories, calibrated with a carbon black standard. The samples were run on a 10-adsorption pressure point program between 0.001 and 0.150 P P_0^{-1} with an equilibration time of 10 s. Three subsamples of each basalt were measured to assess sample variation.

Table 5
Comparison and ranking of the carbon dioxide removal (CDR) and agronomic value of each basalt. The RTM results used measured BET surface areas in the simulations. R_{CO_2}, the theoretical maximum CDR, is defined in Eq. (5). Agronomic value indicates the % cost saving per ha resulting from P and K release from the first year of ERW and complimentary reductions to average UK spring wheat P and K fertiliser application of 14.9 and 36.4 kg ha^{-1} respectively predicted.

Material	CDR value				Agronomic value	
	Short term (15 yr) CDR			Short term (15 yr) CDR	P-fertiliser substitution	K-fertiliser substitution
	Value – Total cation flux from column	Value – Subtracting CDR from calcite in column	Rank		% ha^{-1}	% ha^{-1}
Tichum	8.5	8.5	1	86.1%	>100%	>100%
Hillhouse	5.9	5.9	2	82.0%	56%	44%
Oregon	3.4	3.4	3	70.6%	>100%	24%
Blue Ridge	3.2	3.1	4	11.6%	0%	0%
Tawau	3.0	2.9	5	57.0%	66%	1%
Cragmill	1.3	1.0	6	66.6%	26%	2%

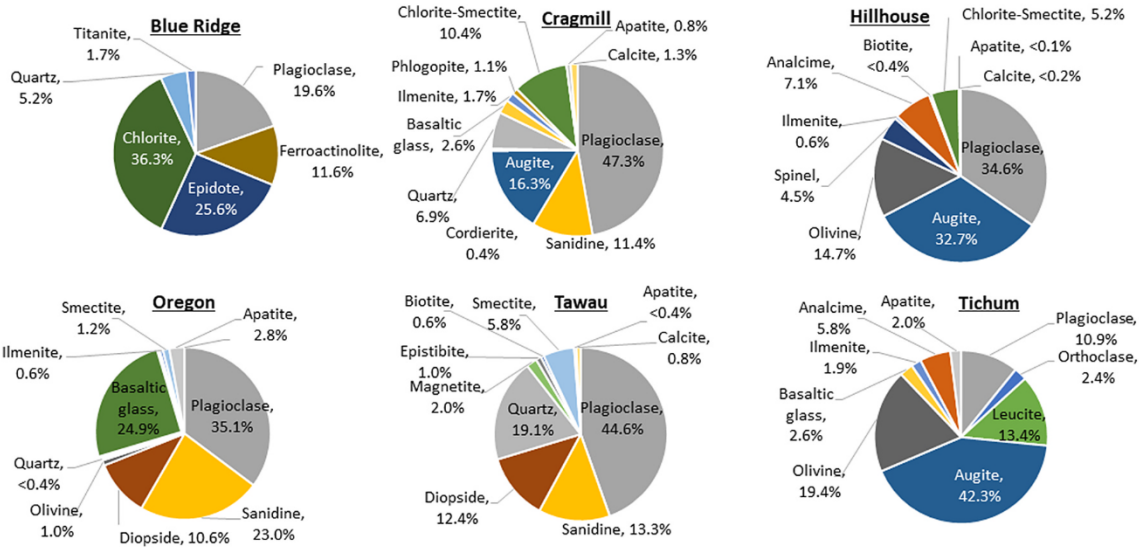

Fig. 2. Mineralogy of basalts studied as determined by XRD analysis. Analyses are given in wt%. For clarity, plagioclase minerals are not differentiated in these pie charts, but chemical analyses (Table S2) identify albite in the Blue Ridge; labradorite in the Cragmill, Hillhouse and Tawau; andesine in the Oregon and Tichum. (For interpretation of the references to colour in this figure legend, the reader is referred to the Web version of this article.)

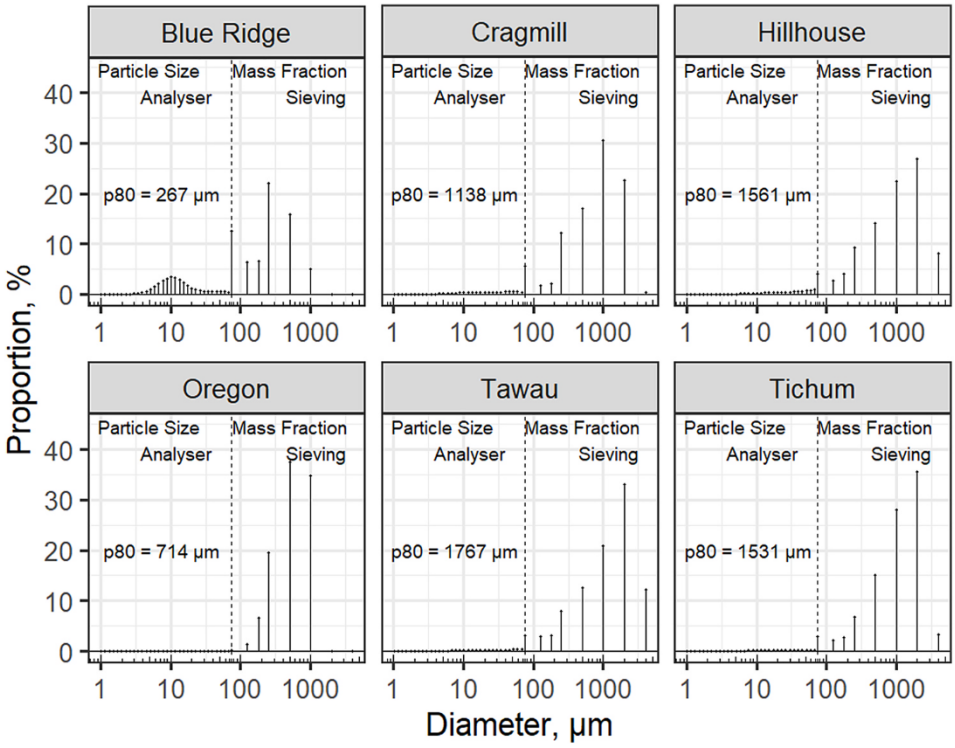

Fig. 3. Basalt particle size distributions, as determined with a particle analyser (<75 µm) ($n \geq 5$ samples per basalt) and from mass fraction sieving (>75 µm) ($n = 4$ samples per basalt). Analysis from the particle size analyser provides the proportion of total concentration of particles, while mass fraction sieving provides the proportion of the total weight. The cumulative density functions for each basalt, from which the *p*80 was determined, are given in the Supplementary Information (Fig. S3).

2.5. Thermogravimetric analysis

Thermogravimetric analyses (TGA) were carried out using a Mettler-Toledo TGA/SDTA851[e] simultaneous thermal analysis system coupled to a Pfeiffer Vacuum ThermoStar mass spectrometer to identify and quantify carbonate minerals present in the basalts. Prior to commencing analyses, the TGA/SDTA system was calibrated using the specified Indium/Aluminium (In/Al) melting test. Zero runs were completed for empty 150 µL platinum crucibles.

For sample analysis, *c.* 75 mg portions of each powdered sample were heated in 150 µL platinum crucibles through a ramped heating program of 30–500 °C at a heating rate of 50 °C/minute, followed by 500–1000 °C at 10 °C/minute, followed by an isotherm at 1000 °C for 10 min to ensure complete reaction. A gas flow of 40 mL min^{-1} N_2 (99.998% pure, not oxygen-free) was maintained throughout. Analyses were controlled and TGA output traces were interpreted using the Mettler STAR[e] software suite. The presence and quantification of the different carbonate species was determined to a high resolution (*c.* 100 ppm/0.01%) by comparison with empirically-derived standard weight losses and temperatures.

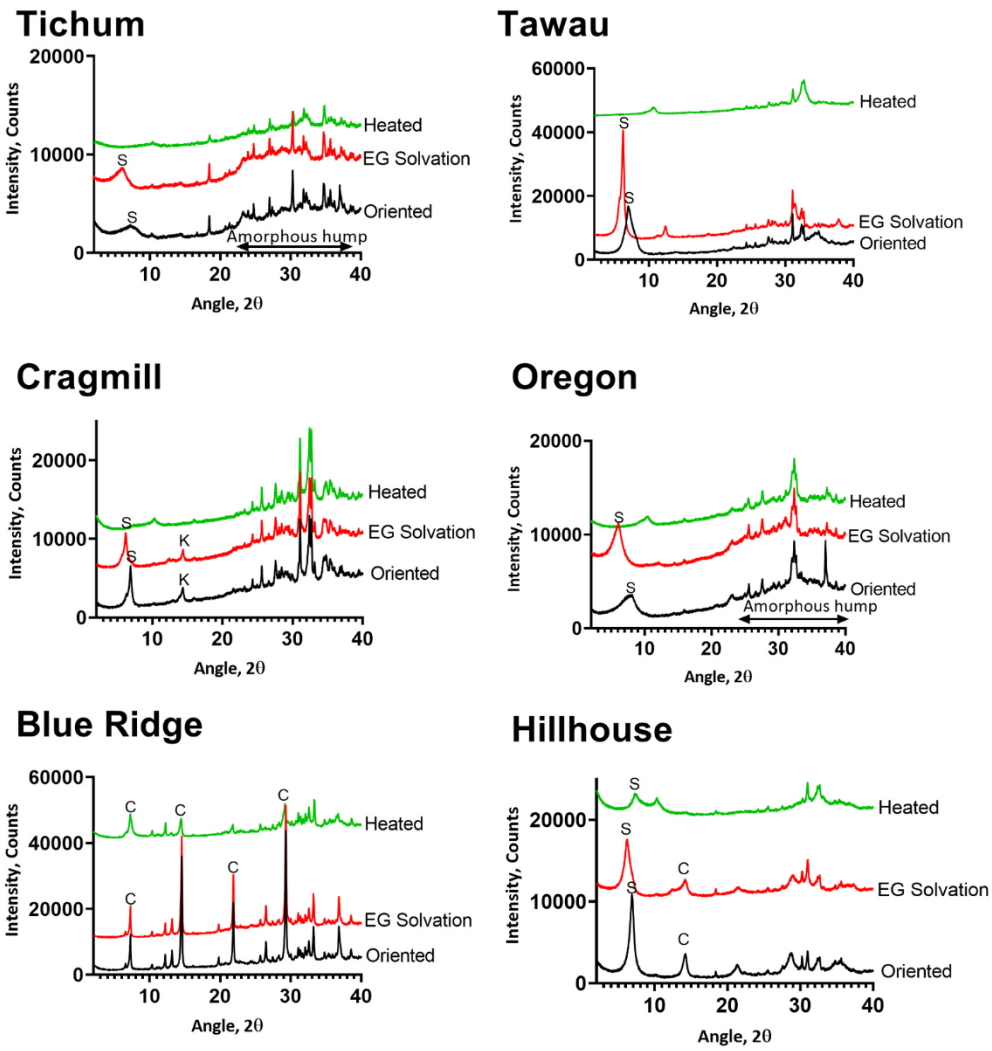

Fig. 4. XRD traces for the clay-sized fraction (<2 μm) of each basalt. Diagnostic clay mineral peaks are labelled: S; smectite, C; chlorite; K; kaolinite.

2.6. Reactive transport modelling

We applied the 1-D reactive transport model (RTM) of Kelland et al. (2020) developed with the PHREEQC (Parkhurst and Appelo, 2013) modelling code and a standard geochemical reaction database (Amm_T&H.dat) (Appelo and Postma, 2004). The model calculates (1) the mass transfer rate of cations from the constituent minerals of the basalt to aqueous solution, (2) the resultant alkalinity release to solution and CDR potential during the initial 15 years of dissolution for each of the six basaltic rocks (Table 1), (3) the projected cumulative CDR after 30 years of basalt dissolution, and (4) P and K release over time via mineral dissolution. The long-term simulations were run for 30 years to account for rapidly weathering minerals dominating dissolution in the initial stages of reaction as well as a longer-term contribution from slower weathering minerals.

We used model parameter sets based on a UK clay loam agricultural soil, described fully in Kelland et al. (2020). The clay-loam soil parameterised RTM was used to simulate 1-D vertical flow and transport, and release of cations from the reactions between basalt and soil solution in a 50 cm deep soil profile, represented as ten 5 cm deep computational cells. Basalt is added in the top 25 cm of the profile to simulate the plough layer mixing depth (Kelland et al., 2020). The 1-D RTM simulates the dissolution of powdered basalt in the top five soil cells (25 cm) equivalent to a field application of 50 tonnes ha^{-1} at 25 °C in an initial mildly acidic soil solution (pH 6.6). The background soil solution is assumed to reflect the background weathering of soil minerals in the absence of basalt amendment, and is also equilibrated with the average annual CO_2 pore gas partial pressure observed at each soil depth in rain-fed maize fields (Nan et al., 2016). The soil profile was assigned an average net infiltration rate of 763 mm yr^{-1} with water filled porosity of 0.2. At each time step (4.9 days), the soil column was replenished with fresh soil solution, of the initial soil pore water composition, entering at the column surface. This flow rate was calculated from irrigation-leachate data over the growth period of the sorghum crop. The biogeochemical sinks for the elements released during weathering are: (1) sorption to solid phases (e.g. cation exchange capacity of clay; sorption to organic matter and to hydrous ferric oxide), (2) reversible precipitation-dissolution of the secondary mineral phases amorphous Al $(OH)_3$, SiO_2 and $Fe(OH)_3$, and (3) the annual uptake of elements (120 days per year) by the sorghum crop.

The proportions of minerals and amorphous material (glass) present in the basalts were determined from normative calculations based on XRD measurements on basalt powder and elemental composition of rock grains based on SEM-EDS analyses, together with TGA determination of the traces of calcite identified in the basalts. We lacked chemical composition data from SEM-EDS analyses on the basaltic glass in the Cragmill basalt, and instead used the formula for basaltic glass taken from Oelkers and Gislason (2001). The chemical kinetic rates of irreversible mineral dissolution were calculated using the generalised rate law for water and acid- and base-catalysed reactions (Eq. (3)) and the

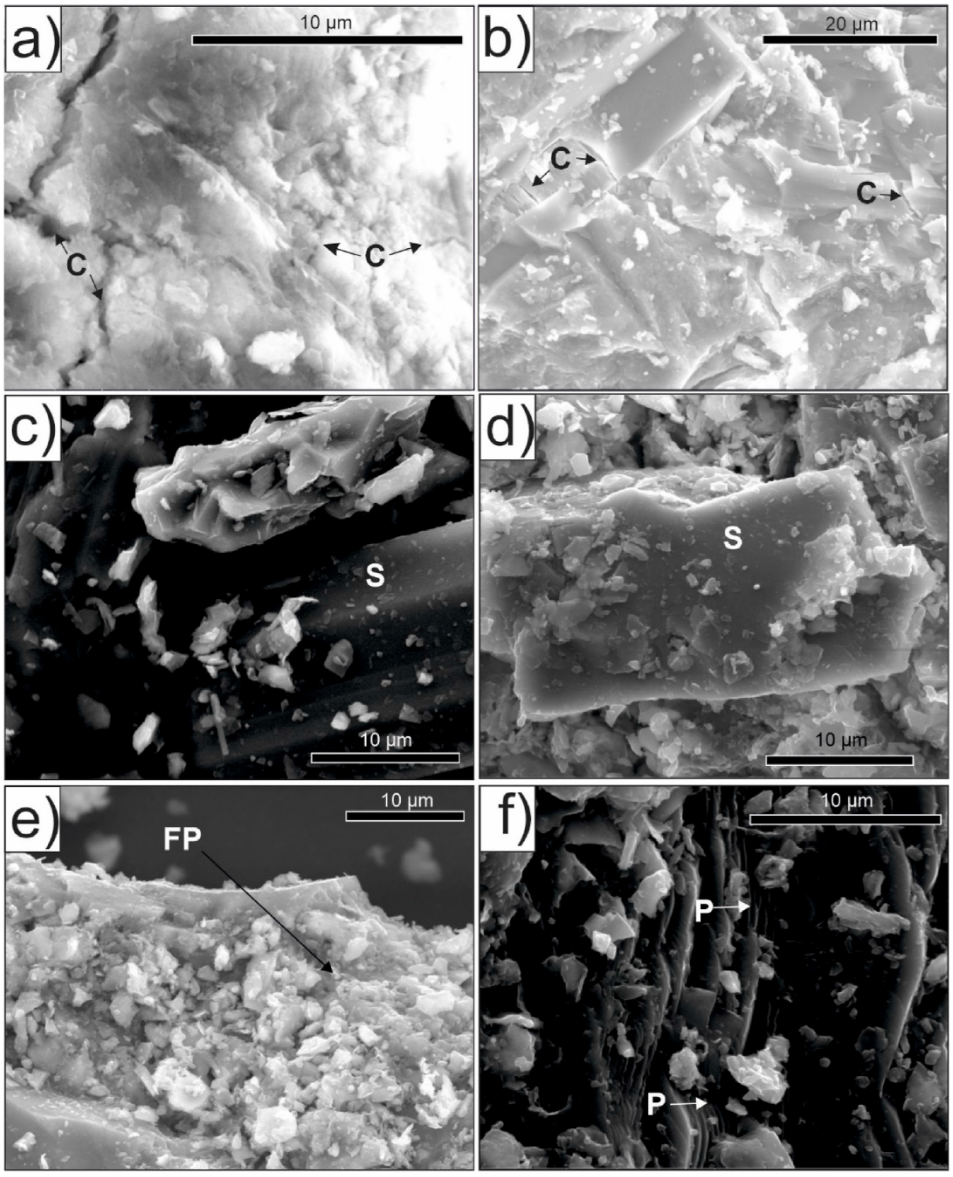

Fig. 5. Secondary Electron Micrographs of materials used in this study. Cracks (denoted C) are shown in grains from the Tichum and Oregon basalts (Fig. 5a and b respectively), compared to relatively smooth grains (denoted S) observed in the Blue Ridge and Cragmill basalts (Fig. 5c and d respectively). High concentrations of fine particles (denoted FP) are observed in the Hillhouse basalt (Fig. 5e) and planar structures (denoted P) in the Tawau basalt (Fig. 5f).

corresponding rate constants taken from the compilation of Palandri and Kharaka (2004) with the exception of basaltic glass. Given the effect of sulphate on Al speciation, and sulphate concentration in the soil pore water, and for consistency with the model used in (Kelland et al., 2020), we used updated rate constants taken from Flaathen et al. (2010) which built upon the rate constants originally developed by Oelkers and Gislason (2001) for the dissolution of glass. The reaction of soil pore fluids with calcite was calculated as thermodynamic mineral solubility equilibria, as calcite has the potential to react reversibly with the solution on timescales considered in this model unlike silicate minerals. The reacting surface area of all kinetic mineral phases was assigned proportionally to their relative abundance in each basalt, however, as an equilibrium phase no reacting surface area term could be attributed to calcite. We used measured (from N_2-BET measurements) SSAs in our simulations, as well as a range of standardised SSAs (i.e. basalt dissolution was modelled using the same surface area for each basalt) from 0.1 to 10 $m^2 g^{-1}$. These standardised surface areas range from the upper-limit of calculated geometric surface areas, calculated from particle size distributions, to the upper BET surface areas identified from our data.

We lacked published dissolution rate laws for the mineral phases titanite, epistilbite, analcime and spinel. However, these minerals contribute only trace quantities of Ca and Mg to the mineral chemical composition of the basalts. Equilibrium constants used to calculate the saturation ratios (SR in Eq. (3)) were sourced from the THERMODDEM database (Blanc et al., 2012) with the exception of those for andesine and labradorite which were taken from (Beaulieu, 2011), augite - which was taken from (Ball and Nordstrom, 1991), and the basaltic glass equilibrium constants which were taken from Aradóttir et al. (2012).

CDR via ERW of crushed basalt applied to soils occurs from alkalinity production as CO_2 released by soil biota respiration dissolves in pore fluids to form carbonic acid. The pore fluids then percolate through the soil and react with silicate minerals to release cations (Ca^{2+}, Mg^{2+}, Na^+, K^+) with concomitant increase in alkalinity, as described in Eq. (1). Transfer of the increased load of cations and alkalinity produced from ERW to the oceans via surface runoff and river transport results in

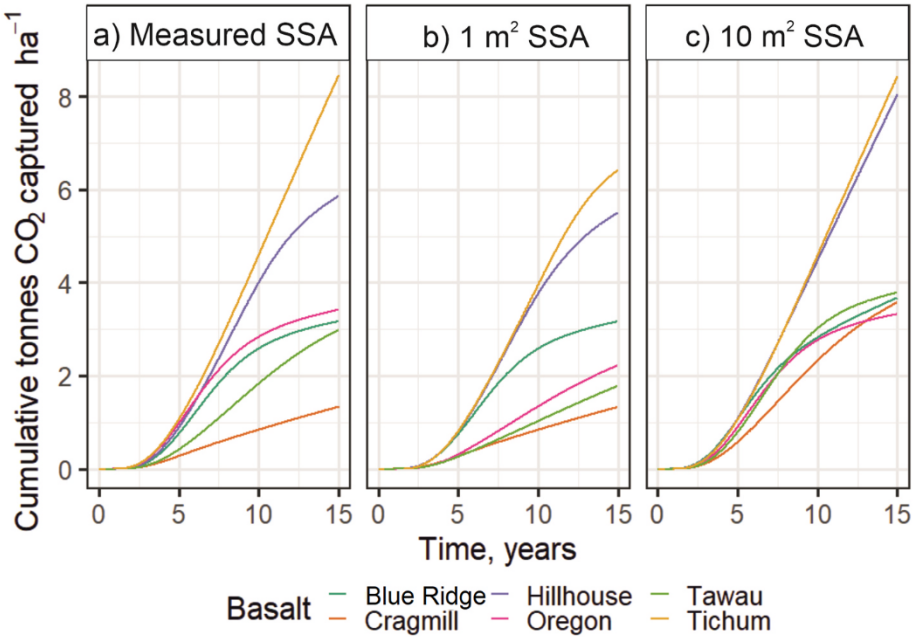

Fig. 6. Cumulative carbon dioxide removal (CDR) after weathering each material over a fifteen-year period under (a) measured specific surface area (SSA) (from BET analyses), (b) a standardised SSA of 1 $m^2 g^{-1}$ and (c) a standardised SSA of 10 $m^2 g^{-1}$. These results do not account for reduced CDR from calcite weathering (Table 3). Potential reductions in CDR are given in Table 5. These results do not account for reduced CDR from calcite weathering (Table 3). Potential reductions in CDR are given in Table 5.

increased marine CDR. Ocean chemistry reduces the CO_2 removal efficiency (η) via this pathway. Based on average ocean temperature (17 °C), salinity (35‰) and dissolved pCO_2 of 400 μatm, η is calculated to equal 0.86, to give 1.72 mol of CO_2 removed per mole of divalent cation added to the ocean (Renforth and Henderson, 2017). The CDR was calculated from the generation of cations in the ERW simulations and removal efficiency, as follows (Eq. (4)):

$$CDR = \eta \cdot \sum(mol\ monovalent\ cations) + 2\eta \cdot \sum(mol\ divalent\ cations) \quad (4)$$

We modelled the dissolution of carbonate phases contained within

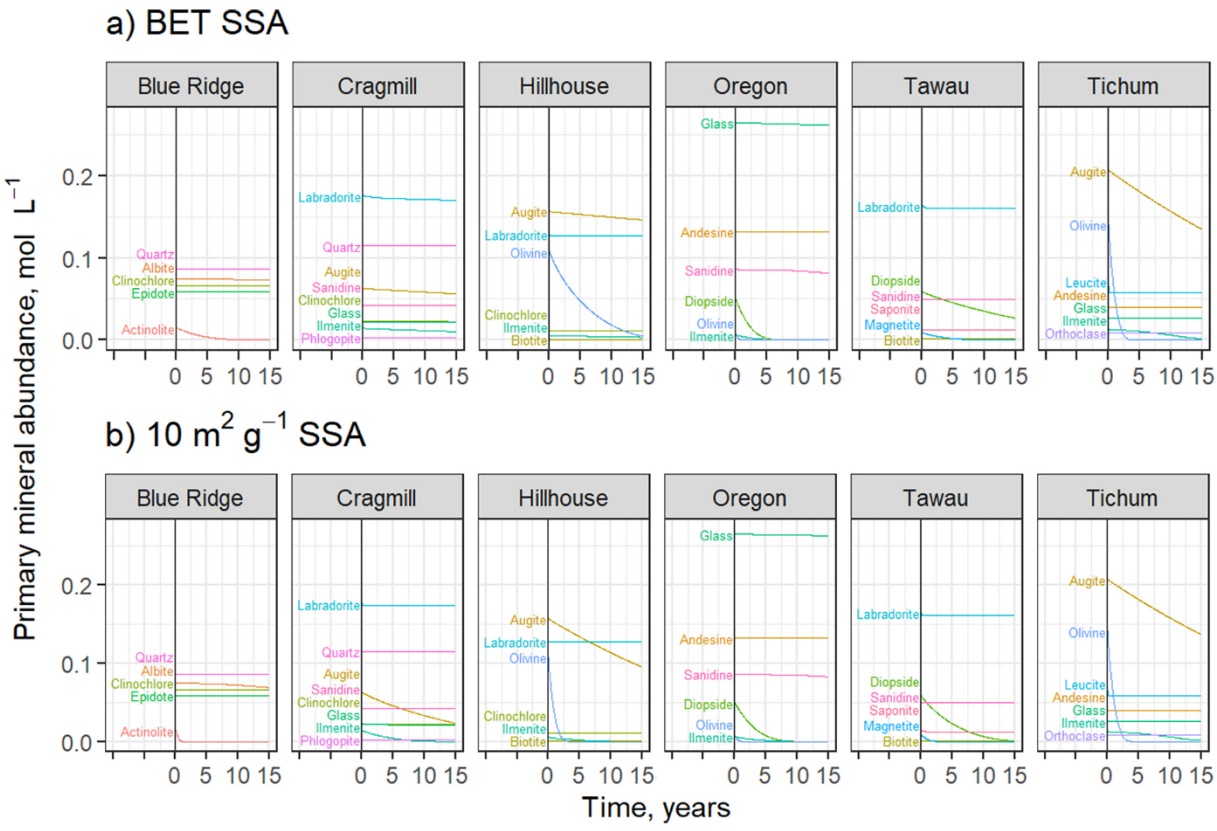

Fig. 7. Modelled mineral concentration of the basalts over time using the (a) measured BET specific surface area (SSA) regime and (b) 10 $m^2 g^{-1}$ SSA. The y axis shows the moles of each mineral phase per unit volume of reacting solution in the soil cells containing basalt with the initial value calculated from XRD analysis. The profiles for smectite (Oregon) and quartz (Tawau and Oregon) were removed from the figure to make the image and labelling clearer and are shown in Fig. S6. These minerals were unreactive under the conditions used in this model.

Table 6
HF-digested ICP-OES whole rock geochemical data expressed as either wt% or mg kg^{-1}. R_{CO_2} values are also given, as calculated from Eq. (5).

Element	Unit	Oregon	Cragmill	Tichum	Blue Ridge	Tawau	Hillhouse
Si	%	22.0	22.0	19.7	19.8	25.0	21.4
Al	%	5.81	5.65	4.91	4.80	6.24	7.00
Ca	%	4.08	5.97	6.28	6.09	4.16	6.72
Mg	%	1.30	1.89	2.80	1.82	1.30	5.86
Fe	%	6.93	8.65	7.91	8.55	4.22	7.11
K	%	2.51	0.844	0.902	0.327	1.47	0.948
Na	%	2.72	1.85	3.18	1.53	1.91	2.31
Ti	%	1.36	1.41	1.32	1.07	0.30	0.85
P	%	0.642	0.129	0.333	0.0862	0.0545	0.108
Mn	%	0.16	0.140	0.137	0.160	0.088	0.123
Ba	%	0.205	0.0317	0.0462	0.0142	0.0219	0.0336
Ce	mg kg^{-1}	83.2	53.3	59.2	<16.0	180.0	<80.0
Co	mg kg^{-1}	18.4	39.2	49.2	49.8	18.6	<40.0
Cr	mg kg^{-1}	34.8	68.1	214.0	154.0	51.4	350.0
Cu	mg kg^{-1}	27.6	52.8	52.4	52.8	27.2	<40.0
La	mg kg^{-1}	33.1	28.4	39.7	<16.0	21.9	<40.0
Ni	mg kg^{-1}	17.8	49.4	192.0	142.0	17.9	195.0
Sr	mg kg^{-1}	296	419	828	209	331	456
V	mg kg^{-1}	398	484	357	409	201	231
Zn	mg kg^{-1}	148.0	144.0	147.0	138.0	70.6	99.2
Zr	mg kg^{-1}	105.0	112.0	144.0	22.4	20.8	<80.0
R_{CO_2} values							
$R_{CO_2\ CaO+MgO}$		0.13	0.20	0.23	0.20	0.14	0.30
$R_{CO_2\ CaO+MgO+Na_2O+K_2O}$		0.16	0.21	0.24	0.21	0.15	0.32

the basalt rock and precipitation of carbonate minerals in the soil and leachate (Eq. (2)) and their effects on CDR. However, on the time scales of the simulations in our study (15 years), there was no net precipitation of carbonate in the soil system.

Possible outgassing of CO_2 during stream water transport (if it occurs) is not considered. However, it would not reduce alkalinity because it does not add or remove any acid. Thus, unless acid is added to the streams, alkalinity will remain conserved while being transported to the marine environment where it ultimately contributes to long-term (~100,000 year timescale) CO_2 removal (Renforth and Henderson, 2017). Carbonate precipitation/dissolution during groundwater transport of weathered products to receiving streams is related to residence time of waters draining arable land, and the presence of carbonate precipitation inhibitors, such as soluble reactive phosphate, suspended material, and dissolved organic matter (Neal, 2002). Further, production of low-molecular-weight organic acids by microbes and root systems could inhibit mineral weathering reactions (Fakhraei and Driscoll, 2015), thus potentially reducing CDR (Taylor et al., 2021). Consideration of these aspects of the carbonate system is beyond the scope of the present 1-D RTM modelling.

We used the simulated mineral dissolution fluxes from the model output to calculate the cumulative release of P and K over time. We calculated the mass transfer of P within the relatively more rapidly dissolving (Palandri and Kharaka, 2004) accessory mineral apatite (identified using XRD, Fig. 1), based on the P content of the rock and the volume of bulk minerals dissolved during each time step. Accessory calcite present in the basalts (Table 3) was treated in the same way, and its potential influence on CDR potential was subtracted from the results retrospectively in Table 5.

3. Results

3.1. Rock type classifications

The chemistry and mineralogy of the basalts from the six sites (Table 1) were compared using Total Alkaline Silica (TAS) (Bas et al., 1986) and Quartz, Alkali feldspar, Plagioclase feldspar and Feldspathoid (QAPF) (Streckeisen, 1974) plots (Fig. 1a and b respectively). Comparisons with both TAS and QAPF classifications confirm that the basalts are generally typical of Large Igneous Provinces (LIPs) (25 locations, of 1354 data points) which host large (>1000 km^3) reserves of basalt (Bryan et al., 2010). According to the TAS classification, Cragmill and Hillhouse are basalts, Oregon and Tichum are basanites and Tawau is a basaltic andesite (Fig. 1a). Under the QAPF scheme, the diverse mineralogy of the six basalts result in Hillhouse and Cragmill being classed as basalt/andesite and Tichum, Oregon and Tawau classed as phonolitic tephrite, latite and dacite, respectively (Fig. 1b). The high silica and quartz concentrations of Tawau (Fig. 1a and b) is typical of its island-arc origin (Table 1). The Blue Ridge metabasalt (Table 1) represents a chlorite-actinolite metabasalt and is unsuitable for both the TAS and QAPF classifications (Robertson, 1999).

3.2. Mineralogical analyses

The detailed mineralogy of the six basalts and chemical composition of minerals derived from SEM-EDS analyses are summarised in Fig. 2 and Table S2 respectively. Basalts produced through crustal extension have a higher proportion of faster weathering minerals (including olivine, augite and plagioclase; Tichum, Hillhouse, Cragmill and Oregon, between 46.7 and 82.0 wt%, Table 2) when compared to those produced at convergent margins (e.g. Tawau) which contain a significant proportion of slower weathering minerals (quartz and hydrothermal clay minerals such as smectite (saponite), 24.9 wt% slow weathering minerals, Table 2). Relative to the other basalts, the Blue Ridge metabasalt has a smaller proportion of fast weathering minerals (19.6 wt%, Table 2).

The relatively fast weathering minerals, Ca/Na-plagioclase and pyroxene, occur in all samples except the Blue Ridge metabasalt (Fig. 1), with abundances varying by a factor of 4–5. Ca/Na-plagioclase in our materials was present as labradorite and andesine (Table S2). The fast-weathering silica-poor feldspathoid, leucite, was present in high concentrations (13.4 wt%, Fig. 2) in the Tichum basalt. Leucite has a significantly higher weathering rate than feldspars (Palandri and Kharaka, 2004; Tole et al., 1986). Olivine, another fast weathering mineral commonly found in basaltic rocks, varied between 1.0 wt% and 19.4 wt % in the Oregon, Hillhouse and Tichum basalts. An XRD-identified amorphous phase, interpreted as fast-weathering basaltic glass from back-scattered electron imaging observations, forms 24.9 wt% of the

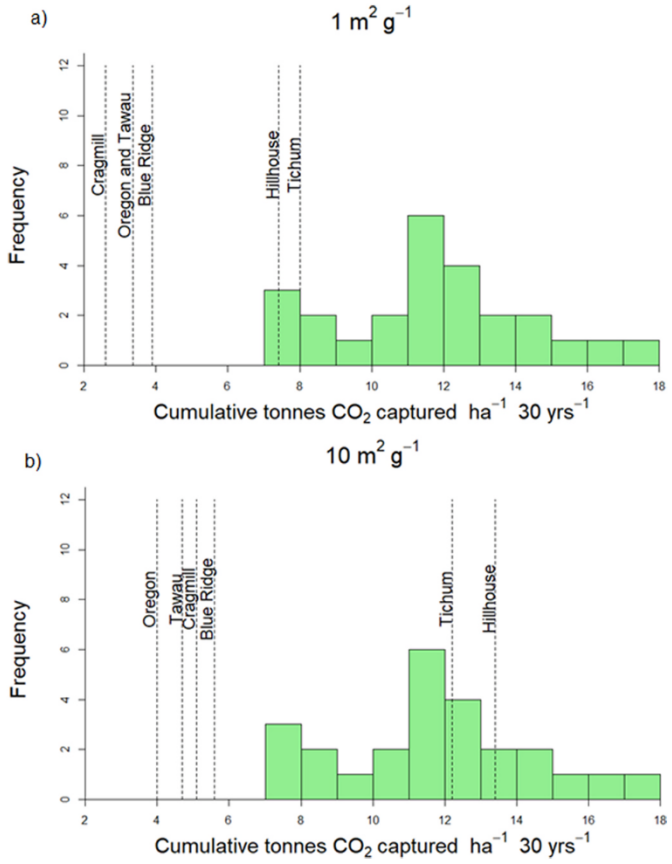

Fig. 8. Histogram showing the predicted CDR potential of basalts from average Ca, Mg, K and Na concentrations of 25 large igneous provinces taken from the GEOROC database (Sarbas, 2008) using (a) a 1 $m^2 g^{-1}$ standardised surface area and (b) a 10 $m^2 g^{-1}$ standardised surface area. The predicted CDR was calculated using $\text{CDR potential} = \exp\left(4.7 + 0.7 \cdot log_{10}(SSA) - \frac{10.6}{\sqrt{R_{CO_2} \cdot 50}}\right)$ (Eq. (6)). This expression is derived from a regression of five basalts across a range of surface areas (0.1 m2g-1–10 m2g-1) and is given in Supplementary Information Fig. S8. Dashed lines show the cumulative carbon capture of the basalts used in this study.

Oregon basalt (Kelland et al., 2020). Fast weathering actinolite, converted from pyroxene during metamorphic reactions (Fyfe et al., 1959) was identified as forming 11.6 wt% of the Blue Ridge metabasalt.

Several medium weathering-rate minerals, formed during metamorphic reactions that convert pyroxenes to epidote and chlorite (Fyfe et al., 1959), are present in the Blue Ridge metabasalt. Additionally, plagioclase was present in the Blue Ridge metabasalt as Na-plagioclase, which dissolves *c.* 2 orders of magnitude slower than the Ca/Na-rich plagioclase minerals observed in all other materials identified in this study. Slower-dissolving K-feldspars, orthoclase and sanidine, vary in abundance between 2.3 wt% and 23 wt% in Tichum, Tawau, Cragmill, and Oregon, but are lacking in the Blue Ridge metabasalt and Hillhouse basalt. Slow-weathering minerals in our basalts comprise quartz and several secondary minerals; quartz was present in the Tawau (19.1 wt %), Cragmill (8.4 wt%) and Blue Ridge (5.2 wt%) basalts. Secondary minerals, such as clays and zeolites, are present in all the samples apart from the Blue Ridge metabasalt. The Cragmill and Hillhouse basalts contain clinochlore (a chlorite group mineral) associated with pyroxene and olivine alteration (Figs. S1 and S2). Saponite (an Fe–Mg smectite, 5.8 wt%) was identified in the Tawau basalt by both XRD and SEM-EDS. Iron oxides identified by XRD as either ilmenite-hematite (Tichum, 1.9 wt%; Cragmill, 1.6 wt%; Hillhouse, 0.6 wt%; Oregon, 0.6 wt%) or magnetite (Tawau, 2.0 wt%) were present in most basalts. SEM-EDS analyses also indicate the presence of an iron oxide phase in the Blue Ridge metabasalt. The Ca–Ti-silicate titanite ($CaTiSiO_5$) comprises 2.0 wt% of the Blue Ridge metabasalt, as confirmed by earlier analysis (USGS, 2019). TGA analysis identified 0.173–1.249 wt% calcite in all six basalts (Table 3).

During mineral dissolution, elements important for plant nutrition including phosphorus (P) and potassium (K) are released into the soil solution (Beerling et al., 2018; Pratt et al., 2020). Apatite, the mineral source of P in the basalts used in our study, is identified in all our samples with the exception of the Blue Ridge basalt, with concentrations varying 28-fold between 0.1 and 2.8 wt%. The essential nutrient K is hosted in K-feldspar (Oregon, Cragmill, Tichum and Tawau), biotite (Hillhouse and Tawau), phlogopite (Cragmill) and leucite (Tichum). The abundance of K bearing minerals varied by two orders of magnitude from 0.6 to 35.1 wt%.

3.3. *Particle sizes, surface area and clay minerals*

Measured particle size distributions (Fig. 3) were used to calculate *p*80 values, i.e. the mesh size through which 80% of particles will pass. These varied by a factor of 10 between the six basalt samples. This wide range reflects differences in the mining and screening (sieving) processes (Table 1) that each quarry site uses to produce the basalt used in our study. The *p*80 values for the Oregon basalt and Blue Ridge metabasalt were smallest because they were passed through finer sieves during production (1.18 and 1.34 mm respectively) compared to the 4–5 mm sieves used for processing the other basalts (Table 1).

BET SSA (Table 4) values generally fall within the range of those reported for commercially available basaltic quarry fines (4.8–10 $m^2 g^{-1}$) (Dalmora et al., 2020; Ponce-Lira et al., 2017; Rigopoulos et al., 2016). These basalts included dolerite mined from the Troodos ophiolite in Cyprus (8.4 $m^2 g^{-1}$) (Rigopoulos et al., 2016), macro-porous basaltic tephra from Mexico (9.6 $m^2 g^{-1}$) (Ponce-Lira et al., 2017), and dacite (4.9 $m^2 g^{-1}$) and andesite (10 $m^2 g^{-1}$) from Brazil (Dalmora et al., 2020).

Clay-sized particles (<2 μm), which comprise a relatively small proportion of each basalt, are likely important controls on the BET SSA. Secondary clay minerals typically have high relative surface areas compared to primary minerals (Brantley and Mellott, 2000; Dogan et al., 2006; Sakizci, 2016), due to their small particle sizes and the accessibility of interlayers and pores to the nitrogen molecules used in the measurements. A small proportion (<0.08%) of clay-sized particles were identified in the basalts through laser particle size analysis. XRD traces of clay-sized separates variously detected chlorite, kaolinite, illite and smectite in the basalts (Fig. 4). The broad peak widths of the smectite basal spacings, particularly shown on the Oregon and Tichum basalt diffraction traces, are indicative of relatively small crystallites (e.g. Moore and Reynolds, 1997) which contribute to their high BET values (14.5 $m^2 g^{-1}$ and 10.3 $m^2 g^{-1}$, respectively). XRD traces of these basalts also show a very broad background curvature between *c.* 25–40°2θ (Fig. 4) indicative of amorphous silicate material with smaller, short range-ordered crystallites with high surface area.

SEM micrographs of representative rock fragments of all six basalts (Fig. 5) show that grain surfaces in the Tichum and Oregon basalts exhibit cracks, the walls of which will contribute to the higher BET surface areas (Fig. 5a and b). In contrast, the Blue Ridge and Cragmill basalts (Fig. 5c and d) have relatively smooth grains. SEM imaging also revealed fine particles adhering to the surface of larger grains of all six basalts, with high concentrations of fine particles observed in the Hillhouse basalt (Fig. 5e) and along planar structures in the Tawau basalt (Fig. 5f). These fine particles (<1 μm diameter) may play a role in BET SSA differences, though their abundance cannot be accurately quantified using the laser particle size analysis because of their small diameter.

We calculated surface roughness (λ) for the six basalts (Table 4) using the measured BET SSA (*S*) and the geometric SSA (*s*) values, which were calculated from the particle size data (Fig. 3). Surface roughness values

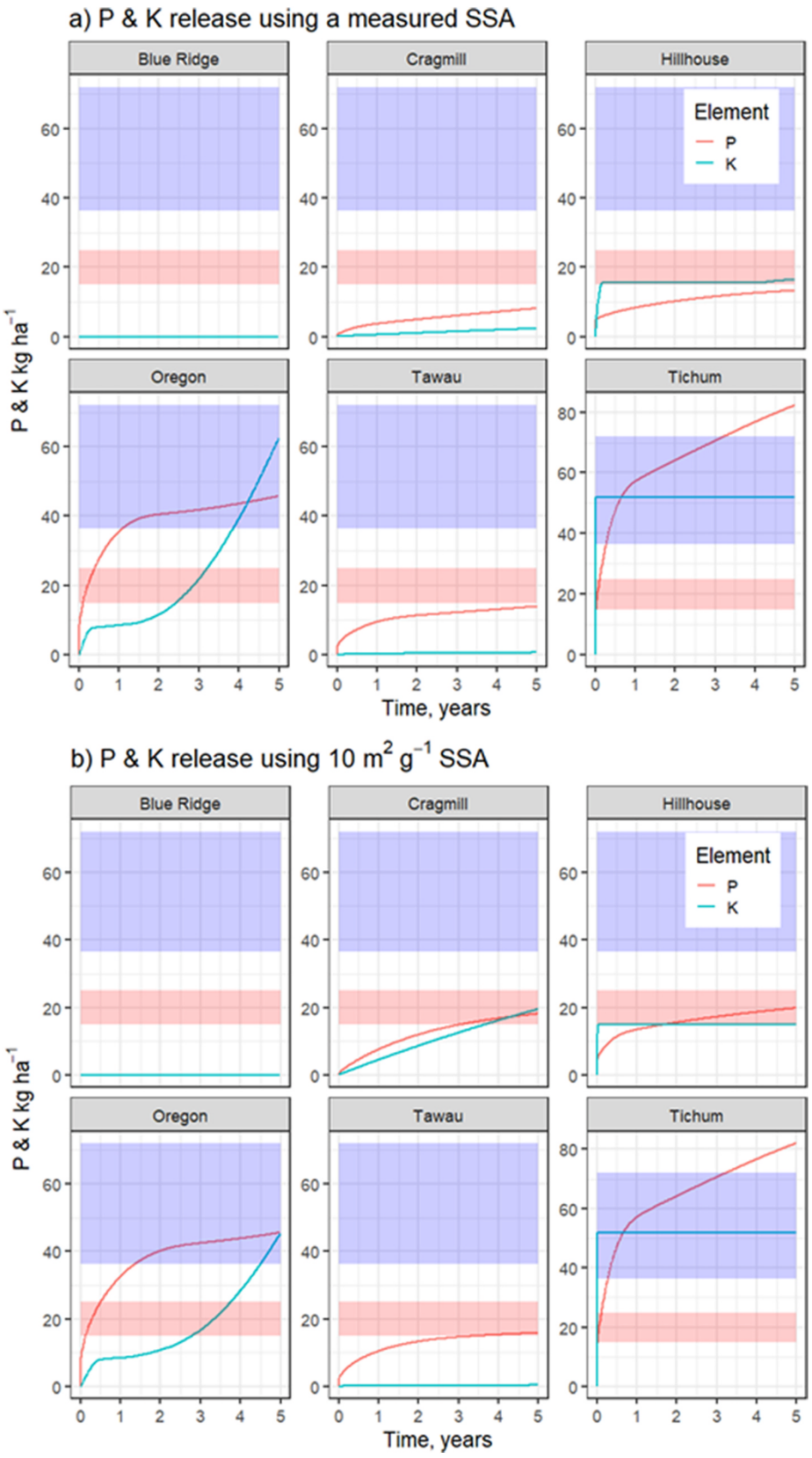

Fig. 9. Cumulative P and K release from the six basaltic materials analysed in this study after 5 years of mineral weathering, as determined from the reactive transport model using (a) measured specific surface area (SSA) (from BET measurements) and using (b) a standardised 10 m^2g^{-1} SSA. Shaded red and blue areas represent average P (14.9–26.2 kg P ha^{-1}) and K (36.4–72.7 kg K ha^{-1}) fertiliser application rates respectively for tillage crops in the UK, based on data from DEFRA (2020). (For interpretation of the references to colour in this figure legend, the reader is referred to the Web version of this article.)

can vary because of differences in the actual shape of particles, grain topography, grain cracking (Hodson, 1998; Hodson et al., 1997; Lee and Parsons, 1995), the presence of fine (<1 μm) particles, and porosity effects. The surface area that is available to potentially react with aqueous solutions increases with surface roughness with, in theory, a proportional increase in dissolution rate. The λ of the six basalts varied by two-orders of magnitude between 13 (Blue Ridge) and 2423 (Oregon) (Table 4). The Oregon and Tichum basalts had the highest BET values

due to the presence of smaller crystallites, inferred from XRD traces of clay-sized separates (Fig. 4), and disrupted surface topography (Fig. 5); they also had the highest λ values. In general, λ values are comparable in magnitude to literature values, e.g., basaltic glass powder with a diameter of 45–125 μm had a λ of *c.* 6–206 after ultrasonic cleaning to remove fine particles (Wolff-Boenisch et al., 2004).

4. Discussion

4.1. RTM simulated CDR from basalts

Our approach was to assess comparative potential CDRs of different basalts used for ERW in relation to mineralogy and surface areas with the same agricultural clay-loam soil; a common soil type in Europe and North America. We recognize different soil types will likely give different responses and our results should therefore be considered illustrative. However, they allow us to compare the CDR potential of each characterised basalt and to assess the relative importance of both mineralogy and surface area for ERW.

RTM simulations are presented assuming the formation of amorphous $Al(OH)_3$, as the secondary mineral sink for Al. This results in higher solution Al concentrations, and little basaltic glass dissolution. Assuming gibbsite formation, as the sink for Al, greatly reduces solution Al concentration, and leads to higher basaltic glass dissolution. Whilst gibbsite can be found in utisols, inceptisols and andisols it is more common as a detectable phase in highly weathered tropical soils and tends to form in Si-poor environments once Si is separated from Al (Huang et al., 2002). Consequently, we use the amorphous Al hydroxide results as our baseline case and report results for the gibbsite case in the Supplementary Information (Figs. S4 and S5).

Calculated CDR potential from our 1-D RTM simulations over 15 years of basalt dissolution following a single application varied widely between 1.3 and 8.5 t CO_2 ha^{-1} for the materials produced by commercial quarries (i.e. using the mineralogy and BET SSA of each of the respective basalts) (Fig. 6a). As expected, the two basalts with the highest CDR potential after 15 years of weathering (Fig. 6a, Hillhouse and Tichum) contained the highest proportion of fast-weathering minerals; olivine, augite and lecuite (Figs. 2 and 7a and b, Tables 2 and 5). Diopside, another pyroxene-group mineral, dissolves most rapidly in the Tawau and Oregon basalts (Fig. 7a and b), and is also present, but in smaller quantities than augite, in the Hillhouse and Tichum basalts (Fig. 1). Actinolite dissolves most rapidly of the metamorphic minerals in the Blue Ridge metabasalt (Fig. 7a and b).

Increasing the surface area in the 1-D RTM of the basalts with measured lower surface areas (i.e., Blue Ridge, Cragmill, Hillhouse and Tawau) to 10 m^2 g^{-1} (as might be achieved by additional milling for example), increased the potential CDR up to three-fold after fifteen years (Fig. 6c), despite surface area increasing by a factor of 4–10. These results suggest that for some basalts, mineralogy and mineral chemistry limit the maximum CDR attainable over short time scales rather than surface area (Table 5). Thus, increasing the surface area for slow-weathering basalts (e.g. through energy intensive grinding) prior to field application in an ERW context may not be warranted in terms of additional gains in CDR.

Our RTM results based on basalt mineralogy and SSA over a 30-year RTM simulation time horizon (Fig. S7) can be compared with the theoretical CDR potential of the same basalts based on their cation content. The 30-year RTM simulation time was used to account for the effects of both the fast- and slow-weathering minerals present in the basalts. Theoretical CDR is described by the term R_{CO_2}, which is defined as the ratio of tonnes of CO_2 captured per tonne of rock mass weathered (Eq. (5)) (Renforth, 2012):

$$R_{CO_2} = \frac{M_{CO_2}}{100}\left(\frac{\%CaO}{M_{CaO}} + \frac{\%MgO}{M_{MgO}}\right)\cdot\omega + \left(\frac{\%Na_2O}{M_{Na_2O}} + \frac{\%K_2O}{M_{K_2O}}\right)\cdot 0.5\omega \quad (5)$$

where M_{CaO}, M_{MgO}, M_{Na_2O}, M_{K_2O} and M_{CO_2} represent the molecular masses of CaO, MgO, Na_2O, K_2O and CO_2 respectively. %CaO, %MgO, % Na_2O and $\%K_2O$ represent the oxide concentrations in the basalt in question and ω represents the additional drawdown from cation flux into the ocean (approximately 1.72). Regression of CDR (Fig. S8), as determined using the RTM simulations over a 30-year time horizon against R_{CO_2} and SSA for five basalts (excluding the Blue Ridge metabasalt) yielded the relationship (Eq. (6), $r^2 = 0.81$, $p = 0.00005$):

$$\text{CDR potential} = \exp\left(4.7 + 0.7\cdot log_{10}(SSA) - \frac{10.6}{\sqrt{R_{CO_2}\cdot 50}}\right) \quad (6)$$

where the CDR potential is expressed in t CO_2 ha^{-1} 30 yrs^{-1} per basalt application with a single baseline application rate of 50 t ha^{-1} at time = 0. R_{CO_2} is calculated from Eq. (5) based on the bulk elemental analyses of the same basalts (Table 6) and SSA is in m^2 g^{-1}. CDR potential therefore represents the maximum value based on 30 years of weathering, and simulated dissolution kinetics demonstrate reduced CDR beyond 30 years (Fig. S7).

We used Eq. (6) to convert the R_{CO_2}, based on widely available (and easily measured) rock chemistry to an equivalent mineralogy-based CDR for a range of initial SSAs. Applying Eq. (6) to the chemical data for 1345 mafic rock samples from 25 LIPs from the GEOROC database (Sarbas, 2008) using a surface area of 1 m^2 g^{-1} predicted a CDR potential range of 3.7–8.5 t CO_2 ha^{-1} 30 yrs^{-1} with a median of 5.8 t CO_2 ha^{-1} 30 yrs^{-1} (Fig. 8a). The Tichum and Hillhouse lie beyond the upper limit of this range, while the Oregon, Blue Ridge, Tawau and Cragmill fall below this range. None of the basalts used in this study fall close to the median predicted CDR of basalts from LIPs. Increasing the surface area to 10 m^2 g^{-1} increased the range of CDR potential of the basalts from the large igneous provinces to between 7.4 and 17.2 t CO_2 ha^{-1}, with a median of 11.7 t CO_2 ha^{-1} (Fig. 8b). Overall, these results display the probable range of CDR of rocks that are classified as basalts, both those that are available commercially and those in large igneous provinces.

4.2. RTM simulated P and K-release

Given the high cost of rock-derived P and K fertilizers (Amundson et al., 2015), we explored the potential for P and K release by basalt weathering to replace them, with the advantage of simultaneously capturing carbon. The P and K concentrations in the basalts studied here varied ten-fold (Table 6), with P hosted primarily in apatite (trace P was also observed in basaltic glass (See Table S2, Kelland et al., 2020; Dontsova et al., 2014; Wolff-Boenisch et al., 2004) and K in K-feldspar (Hillhouse, Oregon, Cragmill, Tichum, Tawau), biotite (Hillhouse and Tawau), phlogopite (Cragmill) and leucite (Tichum). Although the Blue Ridge metabasalt contains P and K (Table 6), no apatite was detected through XRD analyses (Fig. 2) and no K-bearing minerals were detected (Table S2). As a result, no P or K source minerals could be considered in the RTM simulations. For all other basalts, we used the 1-D RTM to simulate P and K release by mineral dissolution with either the BET SSA as the surface area term or a SSA of 10 m^2 g^{-1} (Fig. 9a and b). We plot simulation data for five years, though we refer to the element release rates and cost savings after one year of weathering in this section.

We compared the simulated release rates of P and K with typical annual application rates for arable cropping systems in the UK (Fig. 9a). Average P-fertiliser application rates for tillage crops in the UK (Supporting Information Table S3) range between 14.9 and 26.2 kg P ha^{-1} (DEFRA, 2020), and are 16.6 kg P ha^{-1} in the USA. Wheat, the most widely grown crop in the UK (DEFRA, 2020), is fertilised with an average of either 15 or 25 kg P ha^{-1} depending on when the crop is sown (spring or winter respectively). According to our RTM simulations, weathering of Oregon and Tichum basalts after a year could supply sufficient P for spring wheat in the UK, given BET SSAs. Cragmill,

Hillhouse and Tawau basalts could supply between 26% and 66% of the P provided by conventional fertilisers with a single ERW treatment. Repeated annual ERW rock dust applications could therefore potentially replace relatively more expensive P-fertilisers.

For K, annual fertiliser application rates for major tillage crops in the UK vary between 36.4 and 72.7 kg K ha^{-1} (DEFRA, 2020) (Table S3), with the fertiliser application rate for spring wheat in the UK (36.4 kg K ha^{-1}, DEFRA 2020) and USA (30.6 kg ha^{-1}, USDA 2019) at the lower end. Simulation results demonstrate that, unlike for P, only the Tichum basalt is a major source of K after 1 year of weathering, supplying 53 kg K ha^{-1} (Fig. 9a). This is equivalent to over 100% of UK and USA spring wheat application rates. The Hillhouse and Oregon basalts are also predicted to release K equivalent to significant proportions of K applied as fertiliser after one year of weathering (44% and 24% of the spring wheat K fertiliser rates respectively). The solubility of K-bearing mineral phases is initially limited by the accumulation of dissolution products from relatively rapidly dissolving pyroxenes and olivine (Fig. 7a and b). K-release could therefore likely continue over the long-term, replacing small amounts of K fertiliser over a long period of time.

In addition to wheat production in temperate climates, oil palm plantations in tropical regions represent *c.* 18 million ha of land across the tropical rainforest biome (Skiba et al., 2020) which has an ideal climate (moist and warm) for ERW. Oil palms are fertilised with P and K to improve yield, at recommended rates of up to 14 kg ha^{-1} and 204 kg ha^{-1} respectively (Ng et al., 1999). As a result, our simulations suggest that the 'lower P' basalts (e.g. Hillhouse, Cragmill and Tawau) could substitute P fertilisation. K fertiliser however, which is frequently under applied relative to these recommended rates in Indonesia (Woittiez et al., 2018), still requires substantial application of K fertiliser.

Focusing on P release from basalt amendment, ERW could substitute for P-fertiliser application, reduce costs (Beerling et al., 2018), and reduce reliance on high-grade mineral sources of these elements, over which there has been concern about the long-term sustainability of supplies (Ciceri et al., 2015; Elser and Bennett, 2011). Considering the mass of basalt from eight major volcanic provinces around the world, the average P_2O_5 concentrations from these provinces (Table S4) and assuming that annually 45 million tonnes of P fertiliser, as P_2O_5, is applied globally (Cordell and White, 2014), the global reserve of P in basalt could be used as a fertiliser resource for 2.14 million years. If just 0.05% of this basalt could be sourced as an agricultural rock amendment, basalt could substitute P fertiliser globally for *c.* 425 years.

Conventional P fertilisers cost between \$364–432 US t^{-1} in the UK (AHDB, 2020) and \$406–430 t^{-1} in the USA (Quinn, 2020). Taking the UK average application rate for spring wheat, then the replacement of P fertiliser applications by basalt amendment at 50 t ha^{-1} has a cost offset potential of \$111–432 US t^{-1} P fertiliser in the UK and similar cost savings in the USA at \$99–430 US t^{-1}. An average application rate of 14.9 kg P ha^{-1}, would correspond to savings in the cost of applying basalt powder in the range \$8–29 US ha^{-1}. Considering P fertiliser rates in the USA of 16.6 kg P ha^{-1}, cost savings vary between \$6–26 US ha^{-1}. Fertiliser costs are quoted as \$350 t^{-1} (UK) (AHDB, 2020) and \$363 t^{-1} (USA) (Quinn, 2020). For the K release from the Hillhouse, Oregon and Tichum basalts, the fertiliser savings range between \$79–\$350 US t^{-1} (\$3–\$23 ha^{-1}), depending on the K content of the basalt. Estimated costs for net CDR with ERW on croplands accounting for energy demand and costs of rock mining and grinding, and transportation and spreading costs are approximately *c.* \$170 t^{-1} CO_2 yr^{-1} for the USA and Europe (Beerling et al., 2020). Given approximate net CDR rates of around 4 t CO_2 ha^{-1} for these regions, this yields a cost of CO_2 removed per ha of \$680. Set against these CDR costs, a potential cost offset from supplementing or replacing fertilisers with basalt is relatively small, around *c.* 5%.

5. Conclusions

Detailed mineralogical and chemical analyses of six basalts from a worldwide range of sites are reported and used in 1-D RTM soil profile ERW simulations set-up with an illustrative clay-loam agricultural soil to undertake comparative potential CDR calculations. For a single baseline application rate of 50 t ha^{-1} of crushed basalt, this procedure gives CDR potentials of between 1.3 and 8.5 tonnes of CO_2 ha^{-1} after 15 years of weathering. Faster weathering minerals that are rich in Ca and Mg, such as olivine and augite, dominate CDR potential, particularly during the early stages of dissolution. Selecting basalts with favourable mineralogy and mineral chemistry will be key to optimising the near-term performance of ERW for CDR. Our RTM-predicted CDR potential did not increase linearly with the amount of reactive surface area of rock used in the model, increasing by up to a factor of *c.* 2, despite a factor of 10 increase in surface area. Further processing a basalt (i.e. grinding) to increase its CDR potential therefore also warrants consideration of basalt mineralogy. Simulated P release may be sufficient to fully or partially substitute for typical P fertiliser applications depending on crop type.

Our 1-D RTM approach is based on a real agricultural soil, but does not account for changes in hydrology associated with seasonal changes in precipitation nor replicate P dynamics (i.e. the direct weathering of phosphorus minerals; sorption of P to exchangers) in soils. Ultimately these effects require investigation with further detailed reactive transport modelling of basalt weathering and interaction with plants and water flow in whole soils throughout the depth of the profile, together with data from field-scale trials of ERW over a period of several years.

Declaration of competing interest

The authors declare that they have no known competing financial interests or personal relationships that could have appeared to influence the work reported in this paper.

Acknowledgements

We thank Neil Bramall and Heather Grieveson (University of Sheffield) for completing the whole rock ICP-OES analyses, Gren Turner and Jeremy Ruston (BGS) for assisting with the SEM-EDS analyses and Ian Mounteney (BGS) for assistance with XRD sample preparation and surface area analysis. Robert Ashurst assisted with the particle size analysis and Mark Lomas provided advice on the calculation of geometric specific surface areas. John Fletcher (BGS) is acknowledged for preparing the polished blocks prior to SEM examination. We also thank the following quarry managers for providing information on the source and production of the basalts: Brian Chai (Onika Quarry SDN BHD), Robert Henderson (Hillhouse Quarry Group), Thomas Vanacore (Rock Dust Local LLC), Rich Affeldt (Central Oregon Basalt Products) and Jeffery Sewell (CEMEX UK). SJK publishes with the permission of the Director, British Geological Survey (UKRI). ALL was funded through the NERC ACCE DTP (NE/L002450/1). We gratefully acknowledge funding through a Leverhulme Trust Research Centre Award (RC-2015-029).

Appendix A. Supplementary data

Supplementary data to this article can be found online at https://doi.org/10.1016/j.apgeochem.2021.105023.

References

Agricultural, Horticultural Development Board, AHDB, 2020. GB Fertiliser Price Market Update May 2020.

Allen, C.C., Gooding, J.L., Jercinovic, M., Keil, K., 1981. Altered basaltic glass: a terrestrial analog to the soil of Mars. Icarus 45, 347–369. https://doi.org/10.1016/0019-1035(81)90040-3.

Amann, T., Hartmann, J., 2019. Ideas and perspectives: synergies from co-deployment of negative emission technologies. Biogeosciences 16, 2949–2960. https://doi.org/10.5194/bg-16-2949-2019.

Amundson, R., Berhe, A.A., Hopmans, J.W., Olson, C., Sztein, A.E., Sparks, D.L., 2015. Soil and human security in the 21st century. Science 80. https://doi.org/10.1126/science.1261071.

Anthony, J.W., Bideaux, R.A., Bladh, K.W., Nichols, M.C., 1995. Handbook of Mineralogy (Volume II- Silica, Silicates. Part 1 and 2). Mineral Data publishing.

Appelo, C.A.J., Postma, D., 2004. Geochemistry, Groundwater and Pollution. CRC press.

Aradóttir, E.S.P., Sonnenthal, E.L., Jónsson, H., 2012. Development and evaluation of a thermodynamic dataset for phases of interest in CO2 mineral sequestration in basaltic rocks. Chem. Geol. 304–305, 26–38. https://doi.org/10.1016/J.CHEMGEO.2012.01.031.

Ball, J.W., Nordstrom, D.K., 1991. WATEQ4F - User's Manual with Revised Thermodynamic Data Base and Test Cases for Calculating Speciation of Major, Trace and Redox Elements in Natural Waters. Report No. 90-129. USGS.

Banwart, S.A., Berg, A., Beerling, D.J., 2009. Process-based modeling of silicate mineral weathering responses to increasing atmospheric CO2 and climate change. Global Biogeochem. Cycles 23. https://doi.org/10.1029/2008GB003243.

Bas, M.J.L.E., Maitre, R.W.L.E., Streckeisen, A., Zanettin, B., Rocks, I.S., on the S. of I, 1986. A chemical classification of volcanic rocks based on the total alkali-silica diagram. J. Petrol. 27, 745–750.

Beaulieu, E., 2011. Doctoral Thesis: Modélisation hydrogéochimique des grands bassins fluviaux:Implications du réchauffement climatique. l'Université Toulouse.

Beerling, D.J., Kantzas, E.P., Lomas, M.R., Wade, P., Eufrasio, R.M., Renforth, P., Sarkar, B., Andrews, M.G., James, R.H., Pearce, C.R., Mercure, J.-F., Pollitt, H., Holden, P.B., Edwards, N.R., Khanna, M., Koh, L., Quegan, S., Pidgeon, N.F., Janssens, I.A., Hansen, J., Banwart, S.A., 2020. Potential for large-scale CO2 removal via enhanced rock weathering with croplands. Nature 583, 242–248. https://doi.org/10.1038/s41586-020-2448-9.

Beerling, D.J., Leake, J.R., Long, S.P., Scholes, J.D., Ton, J., Nelson, P.N., Bird, M., Kantzas, E., Taylor, L.L., Sarkar, B., Kelland, M., DeLucia, E., Kantola, I., Müller, C., Rau, G., Hansen, J., 2018. Farming with crops and rocks to address global climate, food and soil security. Native Plants 4, 138–147. https://doi.org/10.1038/s41477-018-0108-y.

Blanc-Betes, E., Kantola, I.B., Gomez-Casanovas, N., Hartman, M.D., Parton, W.J., Lewis, A.L., Beerling, D.J., DeLucia, E.H., 2021. In silico assessment of the potential of basalt amendments to reduce N2O emissions from bioenergy crops. GCB Bioenergy 13, 224–241. https://doi.org/10.1111/gcbb.12757.

Blanc, P., Lassin, A., Piantone, P., Azaroual, M., Jacquemet, N., Fabbri, A., Gaucher, E.C., 2012. Thermoddem: a geochemical database focused on low temperature water/rock interactions and waste materials. Appl. Geochem. 27, 2107–2116.

Brantley, S.L., Mellott, N.P., 2000. Surface area and porosity of primary silicate minerals. Am. Mineral. 85, 1767–1783. https://doi.org/10.2138/am-2000-11-1220.

Brantley, S.L., White, A.F., Hosdson, M.E., 1999. Surface area of primary silicate minerals. In: Jamtveit, B., Meakin, P. (Eds.), Growth, Dissolution and Pattern Formation in Geosystems. Springer, pp. 291–326. https://doi.org/10.1007/978-94-015-9179-9_14.

Brunauer, S., Emmett, P.H., Teller, E., 1938. Adsorption of gases in multimolecular layers. J. Am. Chem. Soc. 60, 309–319. https://doi.org/10.1021/ja01269a023.

Bryan, S.E., Peate, I.U., Peate, D.W., Self, S., Jerram, D.A., Mawby, M.R., Marsh, J.S., Goonie), Miller, J.A., 2010. The largest volcanic eruptions on Earth. Earth Sci. Rev. 102, 207–229. https://doi.org/10.1016/j.earscirev.2010.07.001.

Ciceri, D., Manning, D.A.C., Allanore, A., 2015. Historical and technical developments of potassium resources. Sci. Total Environ. 502, 590–601. https://doi.org/10.1016/j.scitotenv.2014.09.013.

Cordell, D., White, S., 2014. Life's bottleneck: sustaining the world's phosphorus for a food secure future. Annu. Rev. Environ. Resour. 39, 161–188. https://doi.org/10.1146/annurev-environ-010213-113300.

D'Hotman, D., De Villers, O., 1961. Soil rejuvenation with crushed basalt in Mauritius. Int. Sugar J. 63, 363–364.

Dalmora, A.C., Ramos, C.G., Silva Oliveira, M.L., Silva Oliveira, L.F., Homrich Schneider, I.A., Kautzmann, R.M., 2020. Application of andesite rock as a clean source of fertilizer for eucalyptus crop: evidence of sustainability. J. Clean. Prod. 256, 120432. https://doi.org/10.1016/j.jclepro.2020.120432.

Declercq, J., Oelkers, E.H., 2014. CarbFix Report 4 PHREEQC Mineral Dissolution Kinetics Database 5.

DEFRA, 2020. The British Survey of Fertiliser Practice Fertiliser Use on Farm Crops for Crop Year 2019. London.

Dogan, A.U., Dogan, M., Onal, M., Sarikaya, Y., Aburub, A., Wurster, D.E., 2006. Baseline studies of the clay minerals society source clays: specific surface area by the Brunauer Emmett Teller (BET) method. Clay Clay Miner. 54, 62–66. https://doi.org/10.1346/CCMN.2006.0540108.

Dontsova, K., Zaharescu, D., Henderson, W., Verghese, S., Perdrial, N., Hunt, E., Chorover, J., 2014. Impact of organic carbon on weathering and chemical denudation of granular basalt. Geochem. Cosmochim. Acta 139, 508–526. https://doi.org/10.1016/J.GCA.2014.05.010.

Elser, J., Bennett, E., 2011. A broken biogeochemical cycle. Nature 478, 29–31. https://doi.org/10.1038/478029a.

Fakhraei, H., Driscoll, C.T., 2015. Proton and aluminum binding properties of organic acids in surface waters of the northeastern U.S. Environ. Sci. Technol. 49, 2939–2947. https://doi.org/10.1021/es504024u.

Flaathen, T.K., Gislason, S.R., Oelkers, E.H., 2010. The effect of aqueous sulphate on basaltic glass dissolution rates. Chem. Geol. 277, 345–354.

Fyfe, W.S., Turner, F.J., Verhoogen, J., 1959. Fyfe. In: William S. Metamorphic Reactions and Metamorphic Facies, vol. 73. The Geological Society of America, Baltimore.

Gillman, G.P., Burkett, D.C., Coventry, R.J., 2002. Amending highly weathered soils with finely ground basalt rock. Appl. Geochem. 17, 987–1001. https://doi.org/10.1016/S0883-2927(02)00078-1.

Hartmann, J., West, J., Renforth, P., Köhler, P., De La Rocha, C.L., Wolf-Gladrow, D. a, Dürr, H., Scheffran, J., 2013. Enhanced chemical weathering as a geoengineering strategy to reduce atmospheric carbon dioxide, a nutrient source and to mitigate ocean acidification. Rev. Geophys. 51, 113–149. https://doi.org/10.1002/rog.20004.

Hellenbrandt, M., 2004. The inorganic crystal structure database (ICSD)—present and future. Crystallogr. Rev. 10, 17–22. https://doi.org/10.1080/08893110410001664882.

Hillier, S., 1999. Use of an air brush to spray dry samples for X-ray powder diffraction. Clay Miner. 34, 127–135. https://doi.org/10.1180/000985599545984.

Hodson, M.E., 1998. Micropore surface area variation with grain size in unweathered alkali feldspars: implications for surface roughness and dissolution studies. Geochem. Cosmochim. Acta 62, 3429–3435. https://doi.org/10.1016/S0016-7037(98)00244-0.

Hodson, M.E., Lee, M.R., Parsons, I., 1997. Origins of the surface roughness of unweathered alkali feldspar grains. Geochem. Cosmochim. Acta 61, 3885–3896. https://doi.org/10.1016/S0016-7037(97)00197-X.

Huang, P.M., Wang, M.K., Kämpf, N., Schulze, D.G., 2002. Aluminum Hydroxides. Soil Mineral. With Environ. Appl. SSSA Book Series. https://doi.org/10.2136/sssabookser7.c8.

Inorganic Crystal Structure Database (ICSD), 2019. ICSD.

International Centre for Diffraction Data (ICDD), 2019. PDF-4+ 2019 (Database).

IPCC, 2018. Summary for Policymakers of IPCC Special Report on Global Warming of 1.5oC Approved by Governments (Incheon).

Kantola, I., Masters, M.D., Beerling, D.J., Long, S.P., Delucia, E.H., 2017. Potential of global croplands and bioenergy crops for climate change mitigation through deployment for enhanced weathering. Biol. Lett. 13 https://doi.org/10.1098/rsbl.2016.0714.

Kelland, M.E., Wade, P.W., Lewis, A.L., Taylor, L.L., Sarkar, B., Andrews, M.G., Lomas, M.R., Cotton, T.E.A., Kemp, S.J., James, R.H., Pearce, C.R., Hartley, S.E., Hodson, M.E., Leake, J.R., Banwart, S.A., Beerling, D.J., 2020. Increased yield and CO2 sequestration potential with the C4 cereal Sorghum bicolor cultivated in basaltic rock dust-amended agricultural soil. Global Change Biol. https://doi.org/10.1111/gcb.15089 n/a.

Kemp, Simon J., Ellis, M.A., Mounteney, I., Kender, S., 2016. Palaeoclimatic implications of high-resolution clay mineral assemblages preceding and across the onset of the palaeocene–eocene thermal maximum, north sea basin. Clay Miner. 51, 793–813. https://doi.org/10.1180/claymin.2016.051.5.08.

Kemp, S.J., Smith, F.W., Wagner, D., Mounteney, I., Bell, C.P., Milne, C.J., Gowing, C.J. B., Pottas, T.L., 2016. An improved approach to characterize potash-bearing evaporite deposits, evidenced in north yorkshire, United Kingdom. Econ. Geol. 111, 719–742. https://doi.org/10.2113/econgeo.111.3.719.

Kirstein, L.A., Davies, G.R., Heeremans, M., 2006. The petrogenesis of Carboniferous–Permian dyke and sill intrusions across northern Europe. Contrib. Mineral. Petrol. 152, 721–742. https://doi.org/10.1007/s00410-006-0129-9.

Köhler, P., Hartmann, J., Wolf-Gladrow, D.A., 2010. Geoengineering potential of artificially enhanced silicate weathering of olivine. Proc. Natl. Acad. Sci. Unit. States Am. 107, 20228. https://doi.org/10.1073/pnas.1000545107. LP – 20233.

Kristmannsdottir, H., 1979. Alteration of basaltic rocks by hydrothermal-activity at 100-300°C. In: Mortland, M.M., Farmer, V.C.B. (Eds.), International Clay Conference 1978. Elsevier, pp. 359–367. https://doi.org/10.1016/S0070-4571(08)70732-5.

Lackner, K.S., Wendt, C.H., Butt, D.P., Joyce, E.L., Sharp, D.H., 1995. Carbon dioxide disposal in carbonate minerals. Energy 20, 1153–1170. https://doi.org/10.1016/0360-5442(95)00071-N.

Lee, M.R., Parsons, I., 1995. Microtextural controls of weathering of perthitic alkali feldspars. Geochem. Cosmochim. Acta 59, 4465–4488. https://doi.org/10.1016/0016-7037(95)00255-X.

Mercure, J.-F., Pollitt, H., Viñuales, J.E., Edwards, N.R., Holden, P.B., Chewpreecha, U., Salas, P., Sognnaes, I., Lam, A., Knobloch, F., 2018. Macroeconomic impact of stranded fossil fuel assets. Nat. Clim. Change 8, 588–593. https://doi.org/10.1038/s41558-018-0182-1.

Moore, D.M., Reynolds, R.C., 1997. X-Ray Diffraction and the Identification and Analysis of Clay Minerals, Second. OXFORD UNIVERSITY PRESS, New York.

Moosdorf, N., Renforth, P., Hartmann, J., 2014. Carbon dioxide efficiency of terrestrial enhanced weathering. Environ. Sci. Technol. 48, 4809–4816. https://doi.org/10.1021/es4052022.

Nan, W., Yue, S., Li, S., Huang, H., Shen, Y., 2016. The factors related to carbon dioxide effluxes and production in the soil profiles of rain-fed maize fields. Agric. Ecosyst. Environ. 216, 177–187. https://doi.org/10.1016/j.agee.2015.09.032.

Neal, C., 2002. Calcite saturation in eastern UK rivers. Sci. Total Environ. 282–283, 311–326. https://doi.org/10.1016/S0048-9697(01)00921-4.

Ng, H.C.P., Chew, P.S., Goh, K.J., Kee, K.K., 1999. Nutrient requirements and sustainability in mature oil palms - an assessment. Planter 75, 331–345.

Oelkers, E.H., Gislason, S.R., 2001. The mechanism, rates and consequences of basaltic glass dissolution: I. An experimental study of the dissolution rates of basaltic glass as a function of aqueous Al, Si and oxalic acid concentration at 25°C and pH = 3 and 11. Geochem. Cosmochim. Acta 65, 3671–3681. https://doi.org/10.1016/S0016-7037(01)00664-0.

Palandri, J.L., Kharaka, Y.K., 2004. A Compilation of Rate Parameters of Water-mineral Interaction kinetics for Application to Geochemical Modeling. USGS Open File Report. https://doi.org/10.1098/rspb.2004.2754.

Parkhurst, D.L., Appelo, C.A.J., 2013. Description of input and examples for PHREEQC version 3: a computer program for speciation, batch-reaction, one-dimensional transport, and inverse geochemical calculations. US Geol. Surv.

Parry, S.A., Hodson, M.E., Kemp, S.J., Oelkers, E.H., 2015. The surface area and reactivity of granitic soils: I. Dissolution rates of primary minerals as a function of depth and age deduced from field observations. Geoderma 237–238, 21–35. https://doi.org/10.1016/j.geoderma.2014.08.004.

Ponce-Lira, B., Otazo-Sánchez, E.M., Reguera, E., Acevedo-Sandoval, O.A., Prieto-García, F., González-Ramírez, C.A., 2017. Lead removal from aqueous solution by basaltic scoria: adsorption equilibrium and kinetics. Int. J. Environ. Sci. Technol. 14, 1181–1196. https://doi.org/10.1007/s13762-016-1234-6.

Power, I.M., McCutcheon, J., Harrison, A.L., Wilson, S.A., Dipple, G.M., Kelly, S., Southam, C., Southam, G., 2014. Strategizing carbon-neutral mines: a case for pilot projects. Minerals. https://doi.org/10.3390/min4020399.

Pratt, C., Kingston, K., Laycock, B., Levett, I., Pratt, S., 2020. Geo-agriculture: reviewing opportunities through which the geosphere can help address emerging crop production challenges. Agronomy. https://doi.org/10.3390/agronomy10070971.

Quinn, R., 2020. DTN Retail Fertilizer Trends. DTN Progress, Farmer.

R Development Core Team, 2018. A language and environment for statistical computing. R Found. Stat. Comput.

Ramos, C.G., dos Santos de Medeiros, D., Gomez, L., Oliveira, L.F.S., Schneider, I.A.H., Kautzmann, R.M., 2019. Evaluation of soil Re-mineralizer from by-product of volcanic rock mining: experimental proof using black oats and maize crops. Nat. Resour. Res. https://doi.org/10.1007/s11053-019-09529-x.

Renforth, P., 2012. The potential of enhanced weathering in the UK. Int. J. Greenh. Gas Control 10, 229–243. https://doi.org/10.1016/J.IJGGC.2012.06.011.

Renforth, P., Henderson, G., 2017. Assessing ocean alkalinity for carbon sequestration. Rev. Geophys. 55, 636–674. https://doi.org/10.1002/2016RG000533.

Rigopoulos, I., Petallidou, K.C., Vasiliades, M.A., Delimitis, A., Ioannou, I., Efstathiou, A. M., Kyratsi, T., 2016. On the potential use of quarry waste material for CO2 sequestration. J. CO2 Util. 16, 361–370. https://doi.org/10.1016/J.JCOU.2016.09.005.

Robertson, S., 1999. BSG Rock Classification Scheme Volume 2 Classification of Metamorphic Rocks.

Rockström, J., Gaffney, O., Rogelj, J., Meinshausen, M., Nakicenovic, N., Schellnhuber, H.J., 2017. A roadmap for rapid decarbonization. Science 84 (355), 1269. https://doi.org/10.1126/science.aah3443. LP – 1271.

Sabine, P.A., Morey, J.E., Shergold, F.A., 1954. The correlation of the mechanical properties and petrography of a series of quartz-dolerite roadstones. J. Appl. Chem. 4, 131–137. https://doi.org/10.1002/jctb.5010040307.

Sakizci, M., 2016. Investigation of thermal and structural properties of natural and ion-exchanged analcime. ANADOLU Univ. J. Sci. Technol. A - Appl. Sci. Eng. 17 https://doi.org/10.18038/aubtda.266863, 724–724.

Sarbas, B., 2008. The GEOROC Database as Part of a Growing Geoinformatics Network. Geoinformatics 2008—Data to Knowledge. USGS, pp. 42–43.

Seifritz, W., 1990. CO2 disposal by means of silicates. Nature 345. https://doi.org/10.1038/345486b0, 486–486.

Skiba, U., Hergoualc'h, K., Drewer, J., Meijide, A., Knohl, A., 2020. Oil palm plantations are large sources of nitrous oxide, but where are the data to quantify the impact on global warming? Curr. Opin. Environ. Sustain. 47, 81–88. https://doi.org/10.1016/j.cosust.2020.08.019.

Smith, G.A., Hayman, G.A., 1987. Geologic Map of the Eagle Butte and Gateway Quadrangles, Jefferson and Wasco Counties. Oregon, State of Oregon, Department of Geology and Mineral Industries.

Stephenson, P.J., McDougall, I., Hopkins, M.S., Graham, A.W., Collerson, K.D., Johnson, D.P., 2007. Temporal development of the atherton basalt province, north queensland AU - whitehead, P. W. Aust. J. Earth Sci. 54, 691–709. https://doi.org/10.1080/08120090701305236.

Streckeisen, A., 1974. Classification and nomenclature of plutonic rocks recommendations of the IUGS subcommission on the systematics of Igneous Rocks. Geol. Rundsch. 63, 773–786. https://doi.org/10.1007/BF01820841.

Strefler, J., Amann, T., Bauer, N., Kriegler, E., Hartmann, J., 2018. Potential and costs of carbon dioxide removal by enhanced weathering of rocks. Environ. Res. Lett. 13, 34010. https://doi.org/10.1088/1748-9326/aaa9c4.

Tahir, S., Musta, B., Rahim, I.R., 2010. Geological heritage features of Tawau volcanic sequence. Sabah. Bull. Geol. Soc. Malaysia 56, 79–85.

Taylor, L.L., Driscoll, C.T., Groffman, P.M., Rau, G.H., Blum, J.D., Beerling, D.J., 2021. Increased carbon capture by a silicate-treated forested watershed affected by acid deposition. Biogeosciences 18, 169–188. https://doi.org/10.5194/bg-18-169-2021.

Taylor, L.L., Quirk, J., Thorley, R.M.S., Kharecha, P.A., Hansen, J., Ridgwell, A., Lomas, M.R., Banwart, S.A., Beerling, D.J., 2015. Enhanced weathering strategies for stabilizing climate and averting ocean acidification. Nat. Clim. Change 6, 402.

Tole, M.P., Lasaga, A.C., Pantano, C., White, W.B., 1986. The kinetics of dissolution of nepheline (NaAlSiO4). Geochem. Cosmochim. Acta 50, 379–392. https://doi.org/10.1016/0016-7037(86)90191-2.

USDA, 2019. Fertiliser Use and Price.

USGS, 2019. Catoctin Formation - Metabasalt [WWW Document]. https://mrdata.usgs.gov/geology/state/sgmc-unit.php?unit=VACAZc%3B0, 13 October 2019.

Webmineral Chemical Composition, 2019 [WWW Document]. http://webmineral.com/chemical.shtml#.XwReFyhKg2w, 13October2019.

Wilson, M., 1989. Igneous Petrogenesis. Springer Netherlands, Dordrecht. https://doi.org/10.1007/978-1-4020-6788-4.

Woittiez, L.S., Slingerland, M., Rafik, R., Giller, K.E., 2018. Nutritional imbalance in smallholder oil palm plantations in Indonesia. Nutrient Cycl. Agroecosyst. 111, 73–86. https://doi.org/10.1007/s10705-018-9919-5.

Wolff-Boenisch, D., Gislason, S.R., Oelkers, E.H., Putnis, C.V., 2004. The dissolution rates of natural glasses as a function of their composition at pH 4 and 10.6, and temperatures from 25 to 74°C. Geochem. Cosmochim. Acta 68, 4843–4858. https://doi.org/10.1016/j.gca.2004.05.027.